Verification of the Wind Induced Dynamic Response of the Svinesund Bridge in the Time Domain by the use of Autoregressive Simulations

Jørgen Fiskum

Abstract

The subject of this thesis is related to verification of wind induced dynamic response of the Svinesund Bridge in the time domain by the use of autoregressive simulations.

This thesis starts by giving a theoretical study in the field of time–series simulation of wind induced dynamic loading, with emphasis on the Schur decomposition by AR model and polynomial approximation. This is a procedure that generates a multivariate wind field velocity vector by decomposing the PSD matrix into the basis of the eigenvectors. The advantages of this method is that very few spectral modes exhibit significant power, meaning that one could truncate the spectral modal matrix only evaluating the m first eigenvectors ($m \ll n$). Another advantage is that each component of the eigenvectors are very regular functions, which is true independent of the analytical model assumed for the PSD function. This allows, by the use of standard finite element procedure for approximating the eigenvectors, the generation procedure, via standard AR model, to only require a limited number of samples of univariate coherent processes to describe the multivariate wind field, and this number is independent of the number of components in the process. Another advantage making use of the regularity of eigenvectors is that only a small number of subdivision frequencies are needed to approximate the eigenvectors in a polynomial form by a standard finite element procedure. All these advantages combines makes this a very computational effective procedure for generation of a multivariate wind field velocity vector.

As a bonus the physical meaning of eigenvectors and eigenvalues of the PSD matrix provides useful information about the stochastic wind process in view of a structural analysis. This because the eigenvalues could be seen as the power of n independent processes $W_1(t), \ldots, W_n(t)$, while the eigenvectors are mode shapes, similar to the structural modes, associated with the wind field velocity.

After the theory is explained an explanation of how the time domain simulations of wind induced dynamic response was created using the NatHaz On-line Wind

Simulator [2] (NOWS) is given. Here a discussion regarding choices made in regard to different inputs to NOWS as well as how the simulated wind field velocities was to be applied onto the FEM. These simulations was then applied to a finite element model of the Svinesund Bridge, created in the computer software Abaqus, using several different strategies. Then results were extracted from the model in the form of accelerations from these simulations. These accelerations along with the simulated wind field velocities was then compared with real measurements obtained when the storm *Per* passed Svinesund Bridge on January 14, 2007.

After comparing many different velocities and accelerations from different simulations to the measured response it was concluded that the *Full in 2 points* simulation with approach z_1 created the best representation of the measured response. The *Full in 2 points* simulation uses a drag coefficient of $C_D = 0.15$ on both the windward and the leeward box girder, while the arch has a drag coefficient of $C_D = 0.8$. The z_1 approach indicate that the z-coordinates should be given as if the surface is raising linearly between the sea and the arch abutments, and between each arch abutment and pier 5 and 8. NOWS seems to assume that the terrain under a structure is plane, and therefore seems to use the z-coordinates for both defining the height of a point and the spatial separation between to points. So when z_1 was the most correct approach this would indicate that getting the correct height of each point in a simulation is more important than getting a correct spacial representation of the nodes. It was also concluded that exposure category A and B are ill suited for this location, but that it was difficult concluding which was the better of C and D.

In the last chapter sources of error and possible improvements were discussed. Here errors such as not having done a thoroughly calculation of the modulus of elasticity for the arch, taking possible cracking of the concrete into account, which could have great impact on the model were noted. The problems of working with a black box such as the NOWS was also discussed. The summation of this discussion being that if one are to do any improvements the first two considered should possibly bee the modulus of elasticity the concrete arch and finding a different simulation procedure where more controll could be obtained in how the simulation is preformed, either by writing one's own or by finding an open source approach somewhere.

Norsk sammendrag

Temaet for denne masteroppgaven er knyttet til verifisering av vindindusert dynamisk respons av Svinesundsbrua i tidsplanet ved hjelp av autoregressive simuleringer. Masteroppgaven starter med å gi et innblikk i teorien bak simulering av vindindusert dynamisk belastning i tidsplanet, med vekt på Schur dekomposisjon med hjelp av AR-modellering og polynomisk tilnærming. Her blir et vindindusert hastighetsfelt tilnærmet ved at man benytter diverse fordelaktige egenskaper av å faktorisere spektralmatrisen ned til en basis bestående av dens egenvektorer. Dette gjør at man kan trunkere summasjonen fra å gå over n punkter til å gå over m punkter $(m \ll n)$, siden det kun er noen få av egensvingningene som har signifikant amplitude. Også det faktum at de forkjellige komponentene som utgjør egenvektorene er relativt glatte funksjoner kan brukes til å finne en tilnærming til egenvektorene over et stort frekvensspekter ved dele spekteret opp i relativ få deler og tilpasse et polynom i disse punktene. Ved hjelp av vanlig elementmetode til å tilnærme egenvektorene, trengs heller ikke denne genereringsmetoden, via bruk av standard AR modeller, mange en-variable funksjoner for å estimere det mer komplekse vindindusert hastighetsfeltet.

Som en bonus hjelper den fysiske forklaringen av egenvektorer og egenverdier av spektralmatrisen oss til å bedre forstå hvordan vindlaste påvirker konstruksjoner. Dette fordi egenvektorene kan sees på som egensvingningene til vindfeltet, akkurat som egensvingningene til en konstruksjon, mens egenverdiene kan sees på som amplituden til responsen.

Etter denne teoretiske studien beskrives det hvordan en online vind simulator (NatHaz On-line Wind Simulator (NOWS) [2]) ble brukt til å generere vindinduserte hastighetsfeltet for Svinesundsbrua. Deretter følger en diskusjon angående inndataene som benyttes for simuleringen samt hvordan dette simulerte vindfeltet skal påføres elementmodellen i Abaqus. Etter at diverse framgangsmåter ble diskutert og forsøkt, ble simuleringene påført elementmodellen og resultat i form

av akselerasjoner ble hentet ut. Disse ble sammen med hastighetene sammenlignet med målte verdier samlet inn fra sensorer i det stormen *Per* passerte Svinesundsbrua 14. januar 2007.

Etter en rekke sammenligninger kom man fram til at den strategien som ga best tilnærming til de målte verdiene var å beregne en kraft ved bruk av dragkoeffisienten $C_D = 0.15$ for begge kjørebanene i ett, funnet i et vindtunnel-forsøk gjengitt i vedlegg B. Denne kraften ble så påført både den vindutsatte kjørebanen og kjørbanen som lå i le. For buen ble en dragkoeffisient på $C_D = 0.8$. brukt. Simuleringene viste også at det å bruke z-verdier hvor bakken ble antatt å stige lineært fra sjøkanten og opp til beina på buen og fra beina på buen og opp til søyle 5 og 8 ga best resultat av metodene som ble testet. Dette tilsier at det er viktigere at nodene er representert med riktig høyde enn at avstanden mellom nodene trenger å være så nøyaktig. Det ble også vist at eksponeringskategori A og B ikke kan brukes for Svinesundsbrua, men at det var så og svært vanskelig å si hvem av kategori C og D som gir riktigs resultat.

Simuleringene fra NOWS ser også ut til å inneholde mye mindre variasjon enn de målte verdiene. Hva dette kommer av er derimot vanskelig å forklare siden kun teorien bak, men ikke koden brukt for å generere hastighetsfeltene er opplyst for denne simulatoren. Man kan dermed ikke sjekke hvordan simuleringen tilnærmer seg dette. Dessuten er man begrenset til å kun variere noen få utvalgte verdier mellom de forskjellige simuleringene. Dette bringer oss til siste kapittel der feilkilder og forbedringer er diskutert. Her blir nettopp denne 'Black-box'-effekten fra NOWS diskutert. En annen viktig feilkilde er antatt å være utregningen av elastisitetsmodulen til betongsøylen. Fiskum fant i [5] at endringer i betongens elastisitet har stor innvirkning på stivheten til brua, men hverken her eller i [5] er denne variabelen gitt noe prioritet. For videre arbeid bør en risskontroll av betongbuen gjennomføres og buens elastisitetsmodul bør oppdateres ved avvik. Det vil også være en god ide å forsøke å finne alternative simulatorer til NOWS, hvor koden er kjent, evtentuelt skrive en egen simulator. Dette vil gjøre forsøk mer oversiktlig, samt at man har mulighet til å variere mange flere variabler som kan øke nøyaktigheten av simuleringene.

Preface

This thesis constitutes the results of the 10th semester of my master degree program at the Department of Structural Engineering at the Norwegian University of Science and Technology (NTNU), with specialization in Computational Mechanics, and may be seen as a sequel to the project preformed in the course TKT4511 by the undersigned during the fall of 2011 titled; *System identification of constructions - Dynamic response of the Svinesund Bridge.*

The subject of this thesis is related to verification of wind induced dynamic response of the Svinesund Bridge in the time domain by the use of autoregressive simulations. During this work a theoretical study was conducted in the field of time–series simulation of wind induced dynamic load, and a lot of experience was gained in the computer software's Abaqus and Matlab, especially with regard to running time domain simulations and during post-processing of data from these simulations.

I would like to thank Associate Professor Ole Andre Øiseth for all the guidance he has given me, for the advises on where to find relevant literature and for the book loans on subjects of interest. I would also like to thank Associate Professor Anders Rönnquist for his advises and for the loan of important literature.

Jørgen Fiskum

June 22, 2011

Contents

List of Figures

List of Tables

Notation

Most of the notations used in this thesis is described when used, but some commonly used notations are also presented here for convenience

Matrices and vectors:
Matrices are in general written as bold upper case Latin or Greek letters, e.g. $\mathbf{Q}$ or $\boldsymbol{\Psi}$.
Vectors are in general written as bold lower case Latin or Greek letters, e.g. $\mathbf{q}$ or $\boldsymbol{\psi}$.

Superscript and bars above symbol:
Super-script ^{T} indicates the transposed of a vector or a matrix
$Super-script$ * indicates the complex conjugate of a quantity.
A hat ($\wedge$) above a symbol (e.g.$\hat{H}$) indicates normalized quantity
A line (-) above a symbol (e.g.$\overline{U}$) indicates a mean value

Latin letters:
$\hat{Co}$ Denotes the normalized co-spectrum
$E[\cdot]$ Denotes the average value of the variable within the brackets
i Denotes the imaginary unit (i.e. $i = \sqrt{-1}$)
f Denotes frequency given in Hz
PSD Denotes an power spectral density
$\mathbf{S}$ Cross spectral density matrix
S_n Denotes a spectral density
S_{nm} Denotes a cross spectral density
$U(z)$ Instantaneous wind velocity int the main flow direction
$u(x,y,z,t)$ Fluctuating along-wind horizontal velocity component
$v(x,y,z,t)$ Fluctuating across wind horizontal velocity component

$\mathbf{V}(t)$ *n-variate one-dimensional* (*n*-V, 1-D) stochastic vector process containing velocity values at n points

$w(x, y, z, t)$ Fluctuating across wind vertical velocity component

Greek letters:

δ_{pq} Kronecker delta ($\delta_{pq} = 1$ if $p \equiv q$, $\delta_{pq} = 0$ if $p \neq q$).

σ Denotes the standard deviation

$\boldsymbol{\psi}_k$ Denoting the kth eigenvector normalized with respect to the identity matrix

ω Circular frequency given in [rad/s]

$\boldsymbol{\Lambda}$ Diagonal matrix listing the eigenvalues of the PSD matrix

$\boldsymbol{\Psi}$ Spectral matrix containing all the mode shapes$[\boldsymbol{\psi}_1 \dots \boldsymbol{\psi}_k \dots \boldsymbol{\psi}_n]$

Chapter 1

Introduction

The Norwegian Public Roads Administration (NPRA) has been commissioned to investigate the potential for trade and industry, regional employment and settlement patterns of eliminating all ferries along the western corridor (E39) between Kristiansand and Trondheim. Further, this project will explore the technology required for the remaining fjord crossings, including the construction of several new bridges. Some of these will be very slim making wind induced dynamic response a key part of the the design. It is therefore desirable that a control of the accuracy and an assessment of model uncertainty are conducted on the existing computational tools used to calculate wind induced dynamic response. During the construction of the Svinesund Bridge an advanced measurement system was installed measuring wind forces and accelerations, among other things, and at several occasions of strong winds these measurements are stored by the system. One of these occasions occurred when the storm *Per* passed the bridge on January 14, 2007. Data from this storm is in this thesis compared with data from various time domain simulations of wind induced dynamic response.

This thesis constitutes the results of the 10th semester of the master's degree program at the Department of Structural Engineering at The Norwegian University of Science and Technology (NTNU). It may be seen as a sequel to the project preformed in the course TKT4511 by Jørgen Fiskum during the fall of 2011 titled; *System identification of constructions - Dynamic response of the Svinesund Bridge* [5].

The subject of this thesis is related to verification of wind induced dynamic response of the Svinesund Bridge in the time domain by the use of autoregressive

simulations. The Svinesund Bridge is a bridge located on the southern boarder between Norway and Sweden. It consist of two approach bridges supported on piers and a central arch section.

In this thesis a theoretical study in the field of time–series simulation of wind induced dynamic load will be presented. Then time domain simulations of wind induced dynamic response created using the NatHaz On-line Wind Simulator (NOWS) [2] would be given. These simulations will be applied to a finite element model of the Svinesund Bridge, created in the computer software program Abaqus. Accelerations from this model would be extracted and, along with the simulated wind field velocities, be compared with real measurements obtained during the storm *Per*.

At the end of the thesis a discussions on sources of errors and possible improvements would be presented, the latter with work based on this thesis or further studies within this topic in mind.

Chapter 2

Wind basics

2.1 Basics theory concerning wind and wind-statistics

Natural wind is turbulent, especially near ground where friction between the air flow and the terrain causes turbulence. This turbulence varies in a complex, random way in both space and time, making it nearly impossible to accurately model the wind flow. Therefore the wind is described in statistical terms as a stochastic process. This means that the wind itself is seldom measured and instead statistical data is collected from measurements. This data often consist of a mean wind velocity averaged over a 10 minute time frame. To incorporate fluctuations in the wind, the wind velocity is described as the sum of this mean velocity and of fluctuations. Since the fluctuations are random variables they will tend to have zero mean value over a sufficient long period. As the mean wind velocity is usually described as a mean over a 10 minute period, the fluctuating parts are set to have zero mean value over the same period. The notation for the wind velocities at a given time t will in is this paper be:

- In the main flow along-wind direction:

$$U(z) + u(x, y, z, t) \tag{2.1}$$

- In the across wind horizontal direction

$$v(x, y, z, t) \tag{2.2}$$

- In the across wind vertical direction

$$w(x,y,z,t) \tag{2.3}$$

Here the wind velocity in the main flow along-wind direction consists of a mean value, U, that only varies with height above ground and a fluctuating part, u.

2.2   Mean wind velocity

Eurocode 1 gives the following expression for the mean wind velocity above horizontal terrain at an height z above ground

$$U(z) = \begin{cases} U_{bas} \times k_T \times \ln\left(\frac{z}{z_0}\right) & when\ z > z_{min} \\ U_{bas} \times k_T \times \ln\left(\frac{z_{min}}{z_0}\right) & when\ z \leq z_{min} \end{cases} \tag{2.4}$$

Here z_0 is the roughness length, which could be interpreted as the size of a characteristic vortex formed as a result of friction between the air and the ground surface. As seen in eq. 2.4 z_0 coincides with the height at which the mean wind velocity is zero. k_T is the terrain factor, which is affected by the roughness of the surface. U_{bas} is the reference wind velocity, often taken at an height of $10\,\mathrm{m}$. The height z_{min} has been introduced because the velocity profile given in eq. 2.4 has a limited validity close to ground, where turbulence and directional effects prevail.

It should be noted that the term *frictional velocity*, $u_\star$, often is used instead of U_{bas} and k_T, where the frictional velocity is given as $u_\star = U_{bas} \times k_T \times \kappa$. Here κ is the von Kármán constant often taken as 0.4.

2.3   Turbulence

As stated before the wind velocity is described by the mean wind velocity, U, and the turbulence components u, v and w as stated in eq. 2.1 - 2.3. The three turbulence components could be described by their standard deviations, integral length scale, power-spectral density and normalized co-spectra.

2.3.1   Standard deviation

It may be shown that if a zero mean stochastic process is stationary and Gaussian, then its extreme value is proportional to its standard deviation σ_{r_k}, i.e. [15]

$$r_{k_{max}} = \overline{r_k}(x) + k_p \times \sigma_{r_k} \tag{2.5}$$

where k_p is a time invariant peak factor.

Therefore the standard deviation of the turbulence components is of special importance in wind calculations.

The turbulence intensities are defines by [15]

$$I_n(z) = \frac{\sigma_n(z)}{U(z)} \quad where\ n = u, v, w \tag{2.6}$$

For flat terrain the turbulence intensity for the along-wind turbulence component, u, is approximately given by [15]

$$I_u(z) = \begin{cases} 1/\ln(z/z_o)\ when\ z>z_{min} \\ 1/\ln(z_{min}/z_o)\ when\ z\leq z_{min} \end{cases} \tag{2.7}$$

In homogenous terrain up to a height of about $200\,\text{m}$ and not very close to the ground

$$\begin{bmatrix} I_v \\ I_w \end{bmatrix} \approx \begin{bmatrix} 3/4 \\ 1/2 \end{bmatrix} \times I_u \tag{2.8}$$

For height over $200\,\text{m}$ above ground, $I_u \approx I_v \approx I_w$.

2.3.2 Time scales and integral length scale

The auto covariance function $\rho_n(\tau)$, is defined as the normalized mean value of the product of the turbulence component $n = u, v, w$ at time t and at time $t + \tau$ [15]

$$\rho_n(\tau) = \frac{Cov_n(\tau)}{\sigma_n^2} = \frac{E[n(t)\times n(t+\tau)]}{\sigma_n^2} \quad where\ n = u, v, w \tag{2.9}$$

This function indicate how much information a measurement of a turbulence component e.g. $u(x, y, z, t)$ will provide about the value $u(x, y, z, t + \tau)$ measured a time τ later, at the same place.

u may be said to have a characteristic time of memory, the so-called time scale T_n. The time scale may be interpreted as the average duration of a u, v or w wind gust, and is given as

$$T_n = \int_0^\infty \rho_n(\tau) \quad where\ n = u, v, w \tag{2.10}$$

Integral length scales are a measurement of the sizes of the vortices in the wind, or in other words the average size of gust in a given direction. Adopting Taylor's

hypothesis that turbulence convection in the main flow direction takes place with the mean wind velocity (i.e. that flow disturbances travel with the average velocity U), then the average length scales of u, v and w in the x-direction are given by[15]

$$L_n^x = U \times T_n = U \times \int_0^\infty \rho_n(\tau)\,d\tau \quad where\ n = u, v, w \qquad (2.11)$$

2.3.3   Power-spectral density function

While the auto covariance functions represent the time domain properties of the turbulence components, it is the spectral densities that describe the frequency domain properties. This is done because a far more convenient mathematical model of the wind may be established in frequency domain, where the number of unknowns may be decreased considerably without loosing much information.

One of the earliest to come up with a simple and functional function to describe the spectral density was von Kármán in 1948 [17]

$$S_u = \frac{4\hat{f}_u \sigma_u^2}{\left(1 + 70.8 \times \hat{f}_n^{\,2}\right)^{5/6} \times f} \qquad (2.12a)$$

$$S_n = \frac{4\hat{f}_n\left(1 + 755.2\hat{f}_n^{\,2}\right)\sigma_n^2}{\left(1 + 283.2 \times \hat{f}_n^{\,2}\right)^{11/6} \times f} \quad , \quad n = v, w \qquad (2.12b)$$

where $\hat{f}_n = f \times \frac{L_n^x}{U}$, and L_n^x is the integral length scale of the relevant turbulence component.

Later a similar expression was proposed by Kaimal et al. based on data obtained in the 1968 AFCRL Kansas experiments. This expression is easier to fit to relevant data because a parameter A_n as well as the length scales could be changed to fit measurements. The Kaimal spectrum is a simple and commonly used spectrum in wind dynamics and is given as [7]:

$$S_n = \frac{A_n \hat{f}_n \sigma_n^2}{\left(1 + 1.5 A_n \times \hat{f}_n\right)^{5/3} \times f} \quad where\ n = u, v, w \qquad (2.13)$$

A_n may be set to $A_u = 6.8$, $A_v = A_w = 9.4$, unless full scale recordings indicate otherwise.

A further revision of the von Kármán specter was made by Simiu and Scanlan [14]:

$$S_n(z, \omega) = \frac{1}{2} \times \frac{200}{2\pi} \times u_\star^2 \times \frac{z}{U(z)} \times \frac{1}{\left[1 + 50 \times \frac{\omega z}{2\pi U(z)}\right]^{5/3}} \qquad (2.14)$$

where, ω = circular frequency in [rad/s]; $u_\star$ = frictional velocity; $U(z)$ = mean wind velocity at height z.

2.3.4 Spatial properties of wind turbulence

Spatial properties of wind turbulence are obtained measuring recordings simultaneously from two points separated in space. The dependence between points in space is due to the spatial dimension of the vortices in the wind field.

The spatial distribution of the turbulence components is described by the cross-spectrum [15]

$$S_{nn}(r, f) = \int_{-\infty}^{\infty} Cov_{nn}(r, \tau) \times \exp(-2\pi f \tau) \, d\tau \quad , \quad n = u, v, w \qquad (2.15)$$

where $Cov_{nn}(r, \tau)$ is the covariance function and r is the distance between the two points.

In wind engineering the coherence is often used, defined as [15]

$$Coh_{nn}(r, f) = \frac{|S_{nn}|^2}{S_n^2} \qquad (2.16)$$

In eq. 2.16 $|S_{nn}|$ is the real part of the cross-spectrum given as [15]

$$S_{nn}(r, f) = |S_{nn}(r, f)| \exp(i\Phi_{nn}(r, f)) \qquad (2.17)$$

Combining eq. 2.16 and eq. 2.17 the following equation may be derived for the cross-spectrum

$$S_{nn}(r, f) = S_n(f) \times \sqrt{Coh_{nn}(r, f)} \exp(i\Phi_{nn}(r, f)), \quad n = u, v, w \qquad (2.18)$$

Since the wind field is usually assumed homogeneous and perpendicular to the span of the (line-like) structure, phase spectra may be neglected. Because of this the normalized co-spectrum is defined as

$$\hat{Co}_{nm}(r, f) = \frac{Re\left[S_{nm}(r, f)\right]}{\sqrt{S_n(f) S_m(f)}} \qquad (2.19)$$

The normalized co-spectrum $\hat{Co}$ must decrease as the distance r between the two points increases. This decrease depends on the size of the vortices, and a measurement of this size is the ratio between the mean wind velocity and the frequency, U/f.

From the assumption of zero phase-spectrum Davenport suggested from a purely empirical basis, an exponential expression for the normalized co-spectrum [4]

$$\hat{Co}_{uu}\left(r,f\right) = \exp\left(-Crf/U\right) \tag{2.20}$$

where C is a non-dimensional decay constant that determines the spatial extent of the correlation in the turbulence.

This expression was later expanded to be used for two points with transverse separation [4]

$$\hat{Co}_{uu}\left(r_y, r_z, f\right) = \exp\left(-\frac{f}{U}\sqrt{\left(C_y r_y\right)^2 + \left(C_z r_z\right)^2}\right) \tag{2.21}$$

In eq. 2.21 the mean wind velocity is the mean value of the mean wind velocities at the two point considered, $U = \frac{1}{2}\left(U\left(z_1\right) + U\left(z_2\right)\right)$.

Equation 2.20 and 2.21 has the advantage of being simple expression, but incorporates two inconsistencies:

1. The functions are positive for in the entire range of r, and it may be shown that this is in conflict with the definition of zero mean turbulence components.

2. The normalized co-spectrum approaches unity for all r at small frequencies. This is not the case as a wind structure often is characterized by a lack of correlation even at low frequencies.

To prevent these two inconsistencies Krenk derived a modified exponential format allowing for different horizontal and vertical decay constants, C_y and C_z [4]

$$\hat{Co}_{uu}\left(r_y, r_z, f\right) = \left(1 - \frac{1}{2}\frac{f_x}{U}\sqrt{\left(C_y r_y\right)^2 + \left(C_z r_z\right)^2}\right)\exp\left(-\frac{f_x}{U}\sqrt{\left(C_y r_y\right)^2 + \left(C_z r_z\right)^2}\right) \tag{2.22}$$

where the modified frequency f_x is

$$f_x = \sqrt{f^2 + \left(\frac{U}{2\pi L}\right)^2}, \quad L = modified\ length\ scale \tag{2.23}$$

One could then use the known co-spectrum from eq. 2.22, the known autospectrum from eq. 2.13 - 2.12b and eq. 2.19 to find the cross-spectrum

$$S_{nm}(f) = \sqrt{S_n(f) S_m(f)} \times \hat{Co}_{nm}(r_y, r_z, f) \tag{2.24}$$

Another method proposed by Simiu and Scanlan [14], where the coherence function was defined as follows

$$\hat{Co}_{nm}(\omega) = \exp\left[-\frac{\omega}{2\pi} \frac{C_z r_z}{\frac{1}{2}[U(z_n) + U(z_m)]}\right] \times \exp\left[-\frac{\omega}{2\pi} \frac{C_y r_y}{\frac{1}{2}[U(y_n) + U(y_m)]}\right] \tag{2.25}$$

Here C_y and C_z are non-dimensional decay constant generally taken as 10 and 16, respectively, for structural design [1]; $r_z = |z_n - z_m|$ and $r_y = |y_n - y_m|$.

Simiu and Scanlan [14] then defined the cross-spectral density function as

$$S_{nm}(\omega) = \sqrt{S_{nn}(\omega) S_{mm}(\omega)} e^{\left(-\hat{Co}_{nm}(\omega)\right)} \tag{2.26}$$

Chapter 3

Time-domain simulation of wind

3.1 Introduction

For structures in space subject to wind one need to determine the velocity at different points to be able to calculate the load effects due to wind. The wind velocity at a given point in space is usually modeled as a normal stochastic process where the velocity u at the given point depends on the coordinate of the point in space (x, y, z) and on the time t. The stochastic field velocity $u(x, y, z, t)$ is therefore a so called *one-variate four-dimensional* (1-V, 4-D) stochastic field. If one instead only is interested in the velocity in some specific points (say n), one could collect the velocities in the points $u_1(t), u_2(t), ..., u_n(t)$ into a vector $\mathbf{V}(t)$, and then one would have represented the discretized stochastic field by an *n-variate one-dimensional* (*n*-V, 1-D) stochastic vector process. Simulations of normal stochastic vector processes are preformed using two main different approaches [11]:

- Digital simulation based on superposition of harmonic waves with random phase

- Digital simulation obtained as output of digital filters exposed to band-limited white noise input. These numerical schemes are commonly referred to as auto-regressive (AR) algorithms and auto-regressive moving-average (ARMA) algorithms.

In this thesis the AR algorithms are going to be examined closer, by means of the Schur decomposition by AR model and polynomial approximation, as explained in

the papers by Di Paola [11] and Di Paola & Gullo [12].

3.2   Schur decomposition by AR model and polynomial approximation

3.2.1   Stochastic modeling of multivariate wind field

Shown in the papers by Li and Kareem [8][9] one could write the vector process $\mathbf{V}(t)$ as a summation of independent fully coherent stochastic processes as follows:

$$\mathbf{V}(t) = \sum_{k=1}^{n} \mathbf{Y}_k(t) \tag{3.1}$$

where

$$\mathbf{Y}_k(t) = \int_{-\infty}^{\infty} \mathbf{q}_k(\omega) e^{i\omega t} \mathrm{d}B_k(\omega) \tag{3.2}$$

Here $\mathrm{d}B$ are independent orthogonally incremental stochastic processes, that is

$$
\begin{aligned}
E\left[\mathrm{d}B_j(\omega)\right] &= 0, \quad \mathrm{d}B_j(\omega) = \mathrm{d}B_j^\star(\omega) \\
E\left[\mathrm{d}B_j(\omega_r)\,\mathrm{d}B_k(\omega_s)\right] &= \delta_{\omega_r\omega_s}\delta_{jk}d\omega_r
\end{aligned}
\tag{3.3}
$$

where the star denotes complex conjugate and δ_{pq} is the Kronecker delta ($\delta_{pq} = 1$ if $p \equiv q$, $\delta_{pq} = 0$ if $p \neq q$).

$\mathbf{q}_k(\omega)$ are n-vectors such that collecting them in the square matrix $\mathbf{Q}(\omega)$, the following relationship holds:

$$\mathbf{Q}(\omega)\mathbf{Q}^\star(\omega)^T = \mathbf{S}(\omega) \tag{3.4}$$

where $\mathbf{S}(\omega)$ is the PSD matrix:

$$\mathbf{S}(\omega) = \begin{bmatrix} S_{11} & S_{12} & \cdots & S_{1n} \\ S_{21} & S_{22} & \cdots & S_{2n} \\ \vdots & \vdots & \cdots & \vdots \\ S_{n1} & S_{n2} & \cdots & S_{nn} \end{bmatrix} \tag{3.5}$$

here S_{nm} is the cross-spectrum function given in eq. 2.26.

In the case of wind velocity the matrix $\mathbf{Q}(\omega)$ is a real one. There are ∞^n ways to decompose the matrix $\mathbf{S}(\omega)$, so the decomposition in eq. 3.4 is not unique. A different decomposition of the PSD matrix was proposed by Di Paola [11] where

the PSD matrix is decomposed into the frequency-dependent eigenvectors of the PSD matrix itself.

If $\boldsymbol{\psi}_k(\omega)$ is the kth eigenvector normalized with respect to the identity matrix, then by collecting these vectors into a square matrix $\boldsymbol{\Psi}(\omega)$ called the spectral matrix, the following orthogonality conditions hold:

$$\boldsymbol{\Psi}^T(\omega)\boldsymbol{\Psi}(\omega) = \mathbf{I}, \quad \boldsymbol{\Psi}^T(\omega)\mathbf{S}(\omega)\boldsymbol{\Psi}(\omega) = \boldsymbol{\Lambda}(\omega) \tag{3.6}$$

where $\boldsymbol{\Lambda}(\omega)$ is a diagonal matrix listing the eigenvalues of the PSD matrix. The eigenvectors $\boldsymbol{\psi}_k(\omega)$ are real (because the complex part of the cross-spectrum has been neglected) and orthogonal. The digital simulation of the vector $\mathbf{Y}_k(t)$ can then be performed as follows:

$$\mathbf{Y}_k(t) = \int\limits_{-\infty}^{\infty} \boldsymbol{\psi}_k(\omega)\sqrt{\boldsymbol{\Lambda}_k(\omega)}e^{i\omega t}\mathrm{d}B_k(\omega) \tag{3.7}$$

or in the discretized version

$$\mathbf{Y}_k(t) = 2\sum_{j=1}^{N} \boldsymbol{\psi}_k(\omega_j)\sqrt{\Lambda_k(\omega_j)\Delta\omega} \times g_j^{(k)}(t) \tag{3.8}$$

where

$$g_j^{(k)}(t) = R_j^{(k)}\cos(\omega_j t) + I_j^{(k)}\sin(\omega_j t) \tag{3.9}$$

$R_j^{(k)}$ and $I_j^{(k)}$ being zero-mean normal random numbers obeying the following orthogonal relationship:

$$E\left[R_j^{(r)}R_k^{(s)}\right] = \tfrac{1}{2}\delta_{jk}\delta_{rs}, \quad E\left[I_j^{(r)}I_k^{(s)}\right] = \tfrac{1}{2}\delta_{jk}\delta_{rs}$$
$$E\left[R_j^{(r)}I_k^{(s)}\right] = 0 \tag{3.10}$$

So far the procedure for generating the wind velocity vector by decomposing the PSD matrix into the basis of the eigenvectors is shown, but the motivation for doing so is not examined. At this stage it actually seems as much more computational effort is needed for this method compared to a Choleski decomposition. But on the basis of some physical meanings of eigenvalues and eigenvectors the appeal in using the proposed procedure will be revealed in the following section.

3.2.2 Eigen-properties of the PSD matrix of the wind velocities

Di Paola [11] and Di Paola and Gullo [12] uses two examples to explain the physical meaning of eigenvectors and eigenvalues of the matrix $\mathbf{S}(\omega)$. The first one is a case of two points at the same level in the $y - z$ plane, i.e. $S_1 = S_2 = S$. If one uses eq. 2.25 and eq. 2.26 to calculate the coherence and the cross-spectral density function respectively, the matrix $\mathbf{S}(\omega)$ reduces to

$$\mathbf{S}(\omega) = S(\omega) \begin{bmatrix} 1 & e^{-\hat{C}o_{12}(r_y,\omega)} \\ e^{-\hat{C}o_{12}(r_y,\omega)} & 1 \end{bmatrix} \tag{3.11}$$

The eigenvalues of this matrix are

$$\Lambda_1 = S(\omega)\left(1 + e^{-\hat{C}o_{12}(r_y,\omega)}\right) \tag{3.12a}$$

$$\Lambda_2 = S(\omega)\left(1 - e^{-\hat{C}o_{12}(r_y,\omega)}\right) \tag{3.12b}$$

and the corresponding eigenvectors, normalized with respect to the identity matrix, are

$$\boldsymbol{\psi}_1 = \frac{1}{\sqrt{2}} \begin{bmatrix} 1 \\ 1 \end{bmatrix} \tag{3.13a}$$

$$\boldsymbol{\psi}_2 = \frac{1}{\sqrt{2}} \begin{bmatrix} 1 \\ -1 \end{bmatrix} \tag{3.13b}$$

that is for a bivariate wind field velocity the spectral modal matrix $\boldsymbol{\Psi}$ is independent of ω. It follows that, according to eqs. 3.1 and 3.8, one can write

$$\mathbf{V}(t) = 2\boldsymbol{\psi}_1 \sum_{j=1}^{N} \sqrt{\Lambda_1(\omega_j)\,\Delta\omega} \times g_j^{(1)}(t) + 2\boldsymbol{\psi}_2 \sum_{j=1}^{N} \sqrt{\Lambda_2(\omega_j)\,\Delta\omega} \times g_j^{(2)}(t) \tag{3.14}$$

Remembering eq. 3.1 one could think of the summation in eq. 3.14 as two independent processes whose PSD are $\Lambda_1(\omega)$ and $\Lambda_2(\omega)$, respectively; Then eq. 3.14 can be rewritten in the form

$$\mathbf{V}(t) = \boldsymbol{\psi}_1 W_1(t) + \boldsymbol{\psi}_2 W_2(t) \tag{3.15}$$

From eq. 3.15 it can be recognized that for a bivariate wind field velocity two independent (scalar) processes $W_1(t)$ and $W_2(t)$ whose PSD are given in eqs. 3.12a and 3.12b, respectively, can be generated. Then using eq. 3.15, the vector $\mathbf{V}(t)$ is easily generated as the contribution of two fully coherent vectors $\boldsymbol{\psi}_1 W_1(t)$ and $\boldsymbol{\psi}_2 W_2(t)$.

Figure 3.1 shows a plot made in Di Paola and Gullo [12] which show the PSD function $S(\omega)$, written as $S_{v_{11}}$, and the cross PSD function $S(\omega)e^{-\hat{C}o(r_y,r_z,\omega)}$, written as $S_{v_{12}}$, for some given values. This figure also shows a plot of the two functions $\Lambda_1(\omega)$ and $\Lambda_1(\omega)$ given in eqs. 3.12a and 3.12b.

From figure 3.1b one could see that the first eigenvector, having higher power at low frequencies and shape $\boldsymbol{\psi}_1$, is the most important, while the second, having shape $\boldsymbol{\psi}_2$, at low frequency exhibits comparatively small power. Moreover at high frequency both $W_1(t)$ and $W_2(t)$ have the same power.

Using this simple example one could also take a look at the physical interpretation of this analysis method. Assuming the two points considered above are from two anemometers located at the same level on a slender horizontal line-like construction (see fig. 3.2) and Δ is the inter-distance between the two anemometers, then one could by virtue of eq. 3.15 decompose the wind field V_1, V_2 into two independent vector processes $\boldsymbol{\psi}_1 W_1(t)$ and $\boldsymbol{\psi}_2 W_2(t)$. The first one, having the highest power, has for a resultant a vector located at the mid point $\Delta/2$ (visualized in fig. 3.2b), while the second, having the smaller power, constitutes a moment about the z-axis (visualized in fig. 3.2c).

One could then, by virtue of eqs. 3.12a, 3.12b and 2.22, see that if the inter-distance Δ decreases $\hat{C}o(r_y,r_z,\omega) \rightarrow 0$, and then $\Lambda_2(\omega) \rightarrow 0$ and $\Lambda_1(\omega) \rightarrow 2S(\omega)$ which is consistent with the plot in fig. 3.1 for low values of ω. On the contrary, if Δ increases the two independent processes tend to have the same power since $\hat{C}o(r_y,r_z,\omega) \rightarrow 0$ when $\Delta \rightarrow \infty$.

So one could then see the physical significance of eigenvectors and eigenvalues. The eigenvalues are the power of the two independent processes $W_1(t)$ and $W_2(t)$, while the eigenvectors are the mode shapes associated with the wind field velocity. So the bivariate wind field blows as a sum of two independent totally coherent processes associated with blowing shapes just as a structural vibration is decomposed as a sum of independent structural mode shapes. Therefore these processes will hereafter be called *blowing mode shapes* of the wind velocity field.

To show that the above mentioned properties remain unchanged increasing the dimension of the vector $\mathbf{V}(t)$, the second example introduced by Di Paola and
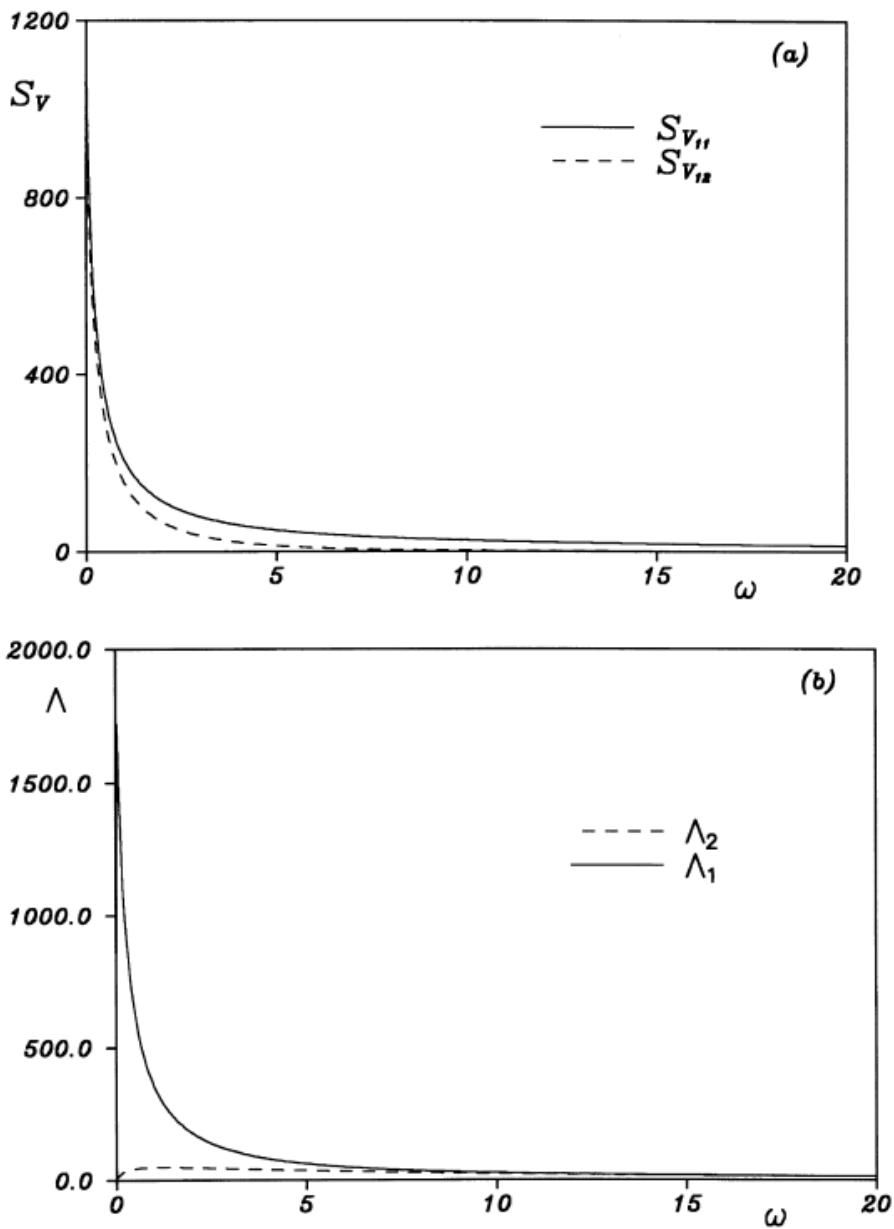
Figure 3.1: Power spectral of bivariate wind field velocity. (a) Elements of the frequency dependent PSD matrix. (b) Frequency dependent eigenvalues $\Lambda_1(\omega)$ and $\Lambda_2(\omega)$. From Di Paola and Gullo [12]
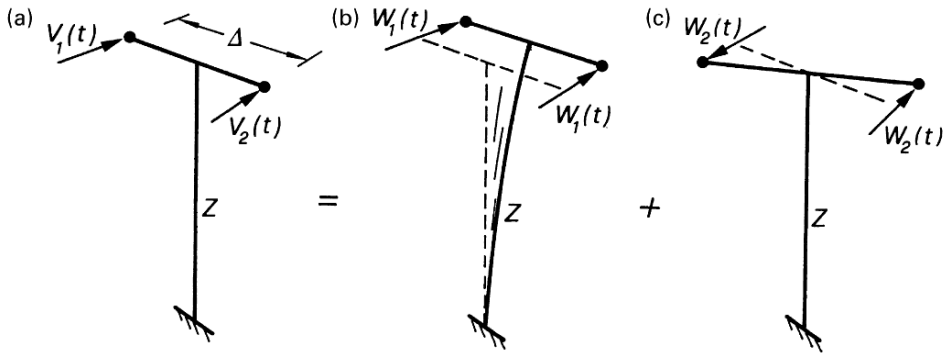
Figure 3.2: Decomposition of bivariate wind velocities. (a) Wind action on two anemometers. (b) First blowing mode shape of wind velocity. (c) Second blowing mode shape of wind velocity. From Di Paola and Gullo [12]
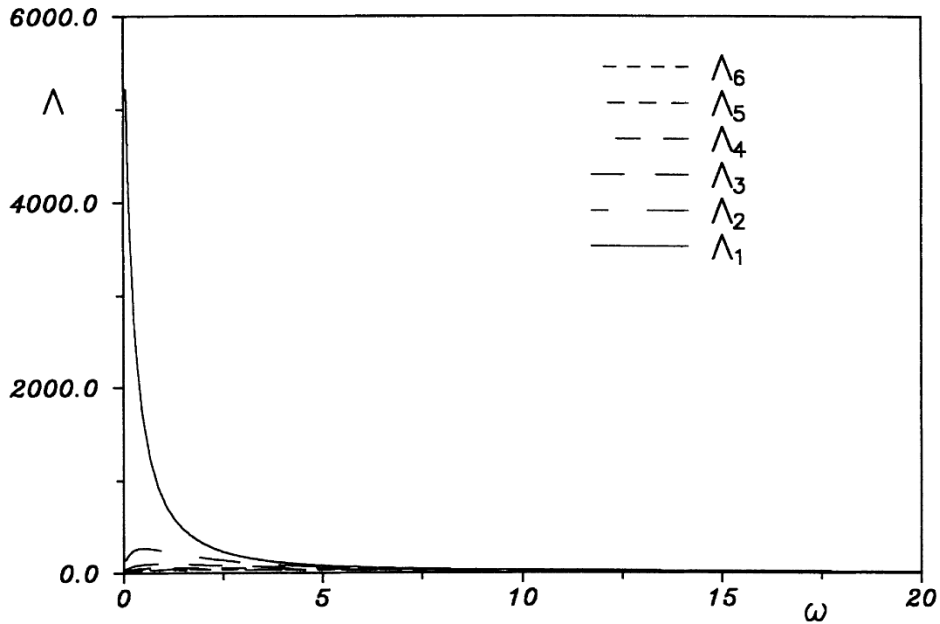
Figure 3.3: Frequency dependent eigenvalues $\Lambda_j(\omega)$ for a six-variate wind field velocity. From Di Paola and Gullo [12]

Gullo [12] was a six-dimensional wind field. Here the points 1-6 are located at different levels having inter-distance of 5 m.

Fig. 3.3 shows the eigenvalues for the six-variate wind field velocity, $\Lambda_j(\omega)$, $j = 1, 2, \ldots, 6$. The eigenvalues are ordered so that $\Lambda_1(\omega) > \Lambda_2 \cdots > \Lambda_6$. This

figure shows that the first blowing mode $\boldsymbol{\psi}_1$ has a significant higher power at low frequencies compared to the other modes. Therefore one could evaluate only the first few eigenvectors, those associated with the higher power, $\Lambda_j(\omega)$, $j = 1, 2, \ldots, m$ ($m \ll n$), and still get a reasonably good answer.

Another interesting discovery is that the components of the eigenvector are very regular functions as seen in fig. 3.4. This means that if one evaluates the actual eigenvector $\boldsymbol{\psi}_j(\omega_k)$ using simple or simultaneous vector iteration methods and uses the initial vector in the iteration $\boldsymbol{\psi}_j(\omega_{k-1})$ as a first attempt, very few iterations are required.

The six-variate wind field also shows good correlation between blowing mode shapes and the structural mode shapes, as suggested in the bivariate example. In fig. 3.5 one could see that the first and sixth blowing mode shapes plotted for different values of ω showing a surprising similarity with the corresponding structural mode shapes. It follows that for a slender structure the contribution on the response of each natural structural mode will be dominated by the corresponding blowing mode shape.

To sum up: The motivation for generating the wind velocity vector by decomposing the PSD matrix into the basis of the eigenvectors is shown, and could be summarized in two key points:

1. Only very few spectral modes exhibit significant power

2. Each component of the eigenvectors is a relative regular function.

By utilizing the first point one could truncate the spectral modal matrix to a summation of only the modes having significant power, say m ($m \ll n$), only evaluating the m first eigenvectors. Because of the second point, using iterative methods for evaluating eigenvalues and eigenvectors, and using the eigenvectors at the previous frequency ω_{k-1} as a first attempt, very few iterations are required in order to compute eigenvalues and eigenvectors at the current frequency ω_k.

3.2.3   Polynomial approximation of eigenvectors

So far it has been shown that the multivariate wind field velocity can be decomposed into a a summation of independent fully coherent multivariate vectors, i.e. one could generate at each time instant t_s a vector $\mathbf{Y}_j(t_s)$ ($j = 1, 2, \ldots, n$) and then by summing the contribution of the various vectors $\mathbf{Y}_j(t_s)$ one gets $\mathbf{V}(t_s)$. A key to the appeal of the decomposition of the PSD matrix in basis of eigenvectors lies in the fact that, according to eq. 3.7, the orthogonal increments $\mathrm{d}B_j(\omega)$ in
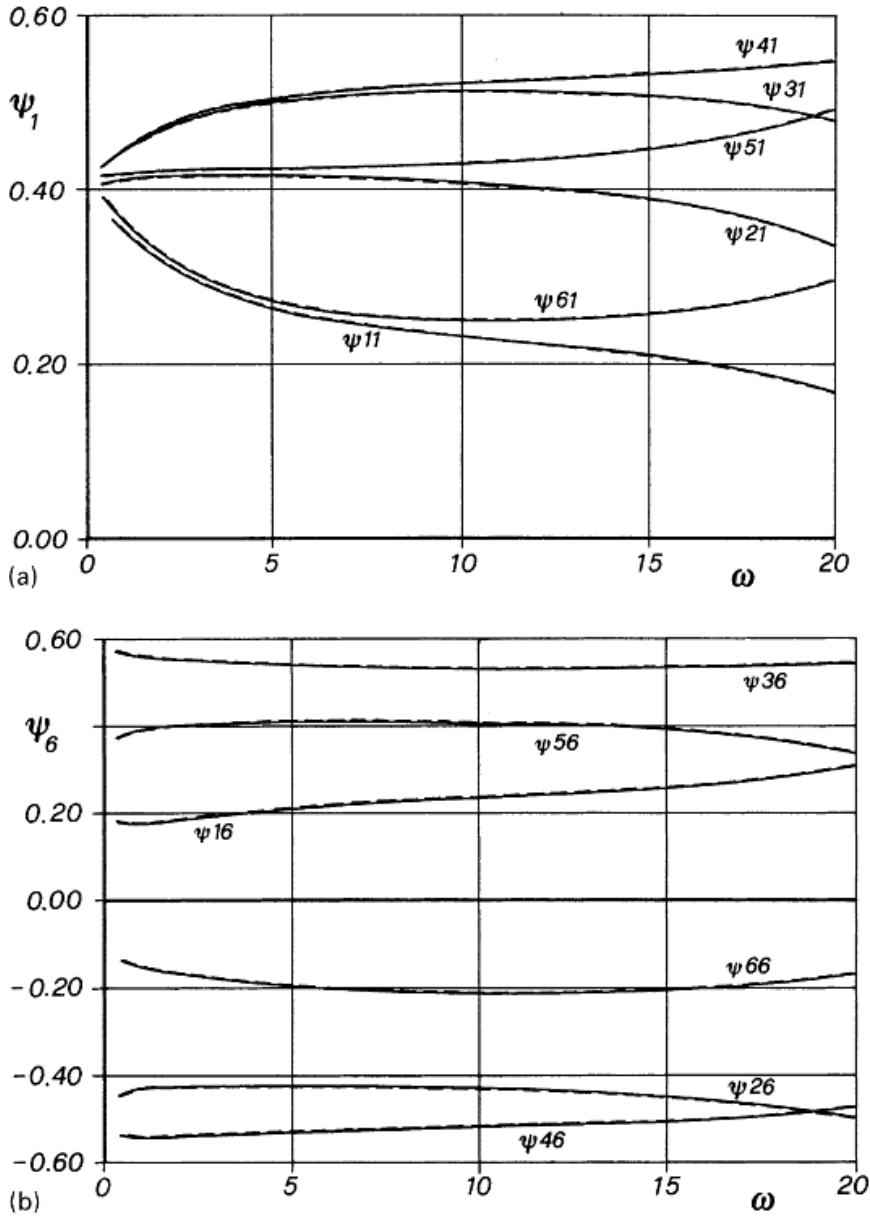
Figure 3.4: Various components of frequency dependent eigenvectors of six-variate wind field velocity: solid line exact; dashed line approximated by third-order polynomial with M=1. (a) First eigenvector. (b) Sixth eigenvector. From Di Paola and Gullo [12]
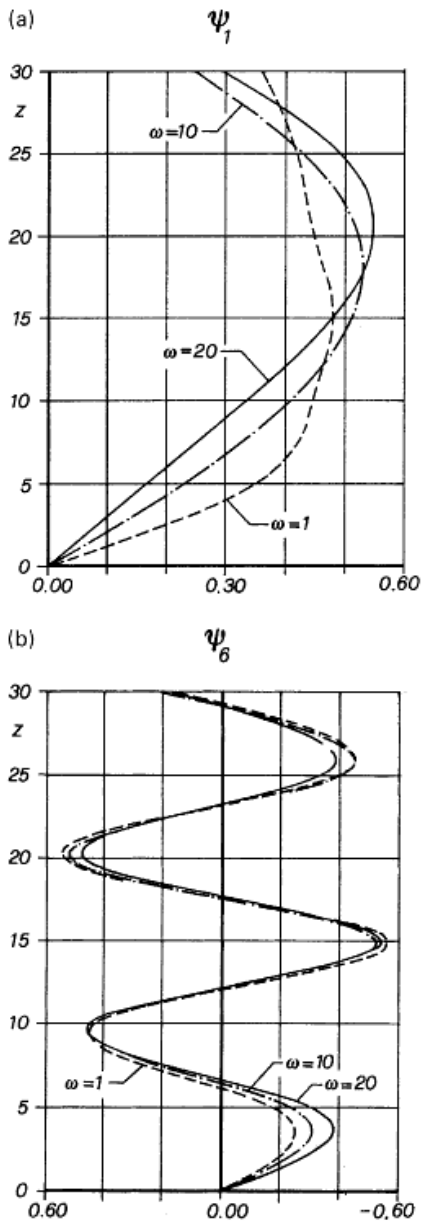
Figure 3.5: Blowing mode shapes of the six-variate wind field velocity. (a) First mode. (b) Sixth mode. From Di Paola and Gullo [12]

the vector $\mathbf{Y}_j(t)$ are scalar ones. In order to take full advantage of this fact for generation purposes by an auto-regressive (AR) model another fundamental step has to be made. If one defines the frequency domain $[\omega_0, \omega_c]$, ω_0 and ω_c being the appropriate lower and upper cut-off frequencies, subdivided into M parts, $\omega_0 \equiv \Omega_0, \Omega_1, \ldots, \Omega_M \equiv \omega_c$. Then the eigenvector $\boldsymbol{\psi}_j(\omega)$ could be approximated in the generic interval $[\Omega_{s-1}, \Omega_s]$ in a polynomial form of fixed order, for example a third order polynomial as suggested by Di Paola and Gullo [12]. Then the sth interval could be approximated as follows

$$\boldsymbol{\psi}_j^{(s)}(\omega) = \mathbf{N}_j^{(s)}\mathbf{l}(\omega), \quad \Omega_{s-1} \leq \omega \leq \Omega_s \tag{3.16}$$

where $\mathbf{l}^T(\omega) = \begin{bmatrix} 1 & \omega & \omega^2 & \omega^3 \end{bmatrix}$. The matrix $\mathbf{N}_j^{(s)}$ (of order $n \times 4$) can be obtained by imposing the continuity at boundaries $\omega_0 \equiv \Omega_{s-1}$ and $\omega_0 \equiv \Omega_s$ and hence one can write

$$\mathbf{N}_j^{(s)} = \overline{\boldsymbol{\Psi}}_j(\Omega_{s-1}, \Omega_s)\, \mathbf{L}_j^{-1}(\Omega_{s-1}, \Omega_s) \tag{3.17}$$

where

$$\mathbf{L}_j(\Omega_{s-1}, \Omega_s) = \begin{bmatrix} 1 & 0 & 1 & 0 \\ \Omega_{s-1} & 1 & \Omega_s & 1 \\ \Omega_{s-1}^2 & 2\Omega_{s-1} & \Omega_s^2 & 2\Omega_s \\ \Omega_{s-1}^3 & 3\Omega_{s-1}^2 & \Omega_s^3 & 3\Omega_s^2 \end{bmatrix} \tag{3.18}$$

and

$$\overline{\boldsymbol{\Psi}}_j(\Omega_{s-1}, \Omega_s) = \begin{bmatrix} \boldsymbol{\psi}_j(\Omega_{s-1}) & \boldsymbol{\psi}_j'(\Omega_{s-1}) & \boldsymbol{\psi}_j(\Omega_s) & \boldsymbol{\psi}_j'(\Omega_s) \end{bmatrix} \tag{3.19}$$

where the prime $'$ denotes differentiation with respect to ω.

Substituting eq. 3.16 into eq. 3.7 one gets

$$\mathbf{Y}_j(t) = \sum_{s=1}^{M} \mathbf{N}_j^{(s)} \int_{\Omega_{s-1}}^{\Omega_s} \mathbf{l}(\omega) \sqrt{\Lambda_j(\omega)} e^{i\omega t} \mathrm{d}B_j^{(s)}(\omega) \tag{3.20}$$

where the orthogonal increments stochastic processes $\mathrm{d}B_j^{(s)}(\omega)$ obey the following relationship

$$E\left[\mathrm{d}B_j^{(s)}(\omega_p)\, \mathrm{d}B_j^{(u)\star}(\omega_q)\right] = \delta_{\omega_p \omega_q} \delta_{su} \mathrm{d}\omega_p \tag{3.21}$$

Hence eq. 3.20 can be written in the form

$$\mathbf{Y}_j(t) = \sum_{s=1}^{M} \mathbf{N}_j^{(s)} \mathbf{U}_j^{(s)}(t) \tag{3.22}$$

where $\mathbf{U}_j^{(s)}(t)$ $(s = 1, 2, \ldots, M)$ are fully coherent four-variate processes independent of each other by virtue of eq. 3.21. So to be able to generate the entire vector $\mathbf{Y}_j(t)$ one would only need to generate $(4 \times M)$ independent univariate processes, instead of an n-variate vector process, each of them given in the form

$$\mathbf{U}_j^{(s)}(t) = \int_{\Omega_{s-1}}^{\Omega_s} e^{i\omega t} \left(\sqrt{\Lambda(\omega)} \begin{bmatrix} 1 \\ \omega \\ \omega^2 \\ \omega^3 \end{bmatrix} \right) dB_j^{(s)}(\omega), \quad s = 1, 2, \ldots, M \tag{3.23}$$

Summarizing so far, the incoherent multivariate process $\mathbf{V}(t)$ is decomposed, by means of eigenvectors of the PSD matrix, as the summation of n fully coherent independent n-variate vectors $\mathbf{Y}(t)$ according to eq. 3.1. Each fully coherent vector $\mathbf{Y}(t)$ could then be, by means of piecewise polynomial approximation of the eigenvectors, decomposed as the summation of M independent fully coherent four-variate vectors according to eq. 3.22.

3.2.4   AR generation

In order to evaluate the generic component $\mathbf{Y}_j(t)$ of the vector $\mathbf{V}(t)$ one have to generate the M independent fully coherent four-variate vectors $\mathbf{U}_j^{(s)}(t)$ defined in eq. 3.23. This could be done using the standard generation via AR model:

$$U_{j,1}^{(s)}(t_k) = \sum_{u=1}^{p} a_{j,u}^{(s)} U_{j,1}^{(s)}(t_{k-u}) + \sigma_{j,1}^{(s)} W_j^{(s)}(t_k) \tag{3.24a}$$

$$U_{j,2}^{(s)}(t_k) = \sum_{u=1}^{p} b_{j,u}^{(s)} U_{j,2}^{(s)}(t_{k-u}) + \sigma_{j,2}^{(s)} W_j^{(s)}(t_k) \tag{3.24b}$$

$$U_{j,3}^{(s)}(t_k) = \sum_{u=1}^{p} c_{j,u}^{(s)} U_{j,3}^{(s)}(t_{k-u}) + \sigma_{j,31}^{(s)} W_j^{(s)}(t_k) \tag{3.24c}$$

$$U_{j,4}^{(s)}(t_k) = \sum_{u=1}^{p} d_{j,u}^{(s)} U_{j,4}^{(s)}(t_{k-u}) + \sigma_{j,4}^{(s)} W_j^{(s)}(t_k) \tag{3.24d}$$

where $a_{j,u}^{(s)}, \ldots, d_{j,u}^{(s)}$ are the parameters of the AR model, $\sigma_{j,r}^{(s)}$ $(r = 1, \ldots, 4)$ are the variances of the input and $W_j^{(s)}(t_k)$ are the normal random variables with zero mean and unit variance, and p is the number of parameters in the filter.

The parameters $a_{j,u}^{(s)}, \ldots, d_{j,u}^{(s)}$ and $\sigma_{j,r}^{(s)}$ $(r = 1, \ldots, 4)$ can be evaluated by the usual Yule-Walker scheme, that is, the autocorrelation method. There one uses the correlation function, $R_{U_{j,r}^{(s)}}$, of $U_{j,r}^{(s)}$ $(r = 1, \ldots, 4)$ which is evaluated as the Fourier transform of $\Lambda_j(\omega)$ in the interval Ω_{s-1}, Ω_s, that is

$$R_{U_{j,r}^{(s)}}(\tau) = \int_{\Omega_{s-1}}^{\Omega_s} \Lambda_j(\omega) e^{i\omega\tau} d\omega \qquad (3.25)$$

To e.g. find the filter parameter $a_{j,u}^{(s)}$ for the first component of $U_j^{(s)}$ one could write

$$R_{U_{j,1}^{(s)}}(t_k - t_l) = \sum_{u=1}^{p} a_{j,u}^{(s)} R_{U_{j,1}^{(s)}}(t_{k-u} - t_l) \qquad (3.26)$$

$$t_l = t_{k-1}, t_{k-2}, \ldots, t_{k-u}$$

Once the filter parameters are found, the standard parameter $\sigma_{j,1}^{(s)}$ of the input can be evaluated by the relationship

$$R_{U_{j,1}^{(s)}}(0) = \sum_{u=1}^{p} a_{j,u}^{(s)} R_{U_{j,1}^{(s)}}(t_k - t_{k-s}) + \sigma_{j,1}^{(s)^2} \qquad (3.27)$$

Similar equations as eqs. 3.25 - 3.27 could be used to find the other components of the vector $\mathbf{U}_j^{(s)}(t)$.

By preforming the AR generation proposed above one have to solve $2(M+1)$ eigenproblems at the end of the interval Ω_{s-1}, Ω_s because the derivatives of the eigenvectors at the end of the intervals are needed. This could be done by evaluating the eigenproblems at the frequencies $\Omega_0 + \delta\Omega, \Omega_1 - \delta\Omega, \ldots, \Omega_M - \delta\Omega$, where $\delta\Omega$ is a very small frequency. One also needs to calculate $4M$ Fourier transforms for the evaluation of the correlation function by means of eq. 3.25. For each vector $\mathbf{Y}_j(t)$ one also needs to find the solution of $4M$ linear systems of p equations for the unknowns in eqs. 3.24a - 3.24d. Once the vector $\mathbf{U}_j^{(s)}(t)$ $(s = 1, \ldots, M)$ is generated, the entire vector $\mathbf{Y}_j(t)$ could be evaluated by eq. 3.22, and then by using eq. 3.1 the vector $\mathbf{V}(t)$ could easily be computed.

3.3   Summation

In this chapter the procedure for generating a multivariate wind field velocity vector by decomposing the PSD matrix into the basis of the eigenvectors was shown. The physical meaning of eigenvectors and eigenvalues of the PSD matrix were discussed, showing that the eigenvalues could be seen as the power of n independent processes $W_1(t), \ldots, W_n(t)$, while the eigenvectors are mode shapes, similar to the structural modes, associated with the wind field velocity.

It was also shown that only a very few spectral modes exhibit significant power, allowing one to truncate the spectral modal matrix retaining only the first few mode shapes. This way the computational effort of the procedure is reduced in a drastic way.

Also shown was the fact that each component of the eigenvectors are very regular functions, which is true independent of the analytical model assumed for the PSD function. This allows, by the use of standard finite element procedure for approximating the eigenvectors, the generation procedure, via standard AR model, to only require a limited number of samples of univariate coherent processes to describe the multivariate wind field, and this number is independent of the number of components in the process.

Another advantage making use of the regularity of eigenvectors is that only a small number of subdivision frequencies are needed to approximate the eigenvectors in a polynomial form by a standard finite element procedure.

In a paper by Ubertini and Giuliano[16]the computational efficiency of this method is proven very good compared to other methods, while at the same time providing good results, given a reasonable choice of model parameters. The same paper also recommends this method since it, in addition to being very computationally efficient, provides useful information about the stochastic wind process in view of a structural analysis.

Chapter 4

Wind velocity simulation on the Svinesund Bridge

4.1 NatHaz On-line Wind Simulator (NOWS)

To preform the wind velocity simulation on the Svinesund bridge the NatHaz On-line Wind Simulator (NOWS) [2] was used. This simulator is based on the theory discussed in chapter 2 and 3.

NOWS utilizes the Simiu and Scanlan method [14] to calculate the power spectral density (eq. 2.14), the coherence function (eq. 2.25) and the cross-spectral density function (eq. 2.26). In the calculation of eq. 3.22 $\left(\mathbf{Y}_j\left(t\right) = \sum_{s=1}^{M} \mathbf{N}_j^{(s)} \mathbf{U}_j^{(s)}\left(t\right) \right)$ a third order polynomial was used in eq. 3.16, as suggestion by Di Paola and Gullo [12]. The number of subdivision frequencies used in eq. 3.22 is $M = 1$, and the order of the AR model used to generate $\mathbf{U}_j^{(s)}\left(t\right)$ in eqs. 3.24a - 3.24d is $p = 4$.

The input to the simulators online user interface is 3-sec gust wind, total number of frequency points and cut-off frequency (which together specify the duration of the simulation), exposure category, and the horizontal and vertical coordinates of the points where the simulation is to be preformed. Before a description and discussion on the chosen input is represented a short description of the Svinesund Bridge and the utilized finite element model (FEM) is given.

4.1.1 The Svinesund Bridge

The Svinesund bridge consists of two approach bridges and a central arch section. The arch section is a central half through arch with span width of 247.30 m. The arch consists of a reinforced hollow concrete box-section where the outside
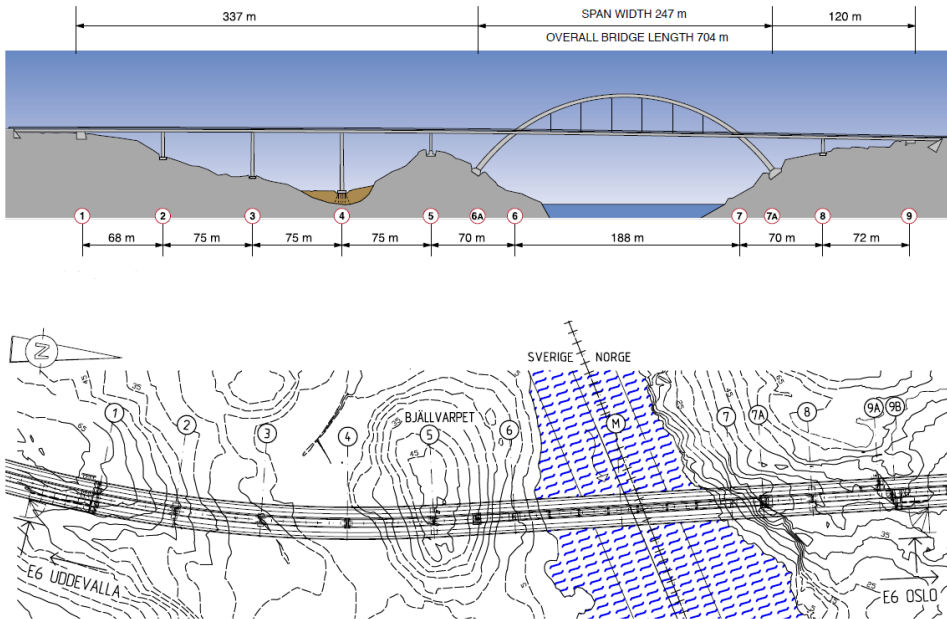
Figure 4.1: Bridge profile and site plan of the Svinesund Bridge. Taken from [3].

height × *width* vary from 7.40 m × 4.20 m at the abutments to 4.00 m × 2.70 m at the crown. The thickness of the box section is 1 m for the vertical walls and 1.4 m for the horizontal ones.

The approach bridges are 337 m long on the Swedish side, 120 m long on the Norwegian side and supported by slender piers of varying heights between 10.69 m and 49.95 m. The entire bridge has an overall length of 704 m. The superstructure of the bridge comprises of two steel box girders each being 11 m wide with a central gap of 5 m.

The superstructure is attached to the arch by a fixed connection at the two junctions between the arch and the superstructure and also suspended in the arch rib by six pairs of hangers (12 in total).

A profile of the bridge along with a site plan is shown in figure 4.1.

The FE-model of the bridge is conducted in the computer software Abaqus and consists of B32 elements, which are 3-node quadratic beams in space, modeled as a wire feature through the shear center of each cross section. To capture the fact that the arch narrows from the abutments to the crown, it is divided into 5 different sections with different cross section measurements. A more detailed description of the bridge and the FE-model could be found in Fiskum [5] and Darholm et al. [3].

4.1.2   3-sec gust wind

Svinesund Bridge has a anemometer installed along with many other instruments used to study the bridge. The measurement system used on the bridge reads this anemometer at a frequency of 50 Hz, and saves the sampled data from 10 minute periods if an predetermined value is exceeded. During the storm Per (January 14, 2007), the measurement system saved 90 of these 10 minute periods, and based on this data a mean 10-minute wind velocity is calculated and used in this thesis. This was done by taking the maximum mean value from these 90 10-minute periods. The result of this calculation was that the 10-minute average wind velocity for this data set was, $\overline{U}_{10} = 23.03 \, \mathrm{m/s}$.

Since the online simulator is based on the American standard ASCE 7-98 it requires the 3-sec gust wind velocity at 10 meters height as a input. This means that the the 10-minute velocity taken near pier 5 at the bridge level needs to be converted to an equivalent 3-sec gust wind velocity at an height of 10 m. To do this a formula which give the the relation between wind speeds averaged over various time intervals, and a mean ratio between wind speeds with different averaging times was used. These are taken from Simiu and Miyata [13] and are given in table 4.1 and eq. 4.1.

$$U_t \left(z \right) = \overline{U} \left(z \right) \left[1 + \frac{\eta c \left(t \right)}{2.5 \ln \left(z/z_0 \right)} \right] \tag{4.1}$$

where $U_t \left(z \right)$ is the speed averaged over t seconds and $\overline{U} \left(z \right)$ is the speed averaged over 1 h for the terrain with surface roughness z_0. The coefficients η and $c \left(t \right)$ may be assumed to have the approximate values given in table 4.2.

These relations give the following formula to convert the 10 minute mean wind at 17 meters above ground to a 3-sec gust wind at 10 meters above ground with $z_0 = 0.025$:

Table 4.1: Mean ratio r of the t-s speed to the hourly speed at 10 m above ground in open terrain. [13]

$t \, (s)$	3	5	40	60	600	3600
r	1.52	1.49	1.29	1.25	1.1	1.0

Table 4.2: Factors $\eta(z_0)$ and $c(t)$. From Simiu and Miyata [13]

$z_0(m)$	0.005	0.03	0.30	1.00						
$\eta(z_0)$	2.55	2.45	2.30	2.20						

t	1	10	20	30	50	100	200	300	600	1000	3600
$c(t)$	3.00	2.32	2.00	1.73	1.35	1.02	0.70	0.54	0.36	0.16	0.00

$$\begin{align}
U_{10}(17) &= \overline{U}(10)\left[1 + \frac{2.47 \times 0.36}{2.5\ln(17/0.025)}\right] \notag \\
\overline{U}(10) &= \frac{U_{10}(17)}{1.0545} \tag{4.2} \\
U_{3-sec}(10) &= \frac{U_{10}(17)}{1.0545} \times 1.52 \implies U_{3-sec}(10) = 1.44 \times U_{10}(17) \notag
\end{align}$$

With a 10-minute average wind velocity set to $U_{10}(17) = 23.03\,\text{m/s}$ this gives a 3-sec gust wind of $U_{3-sec}(10) = 33.2\,\text{m/s}$.

4.1.3   Number of frequency points and cut of frequency

Since the eight first eigenfrequencies found by Fiskum [5] is less than $2\,\text{Hz}$, and a cut of frequency of $2\,\text{Hz}$ gives a reasonable time step, the cut of frequency was set to $f_c = 2\,\text{Hz}$.

The numbers of frequency points where chosen so that the simulation becomes 10 minutes long. This is calculated by the following formula

$$T = 2 \times N \times \Delta t \tag{4.3}$$

where T is the time of the simulation in seconds, N is the number of frequency points and Δt is the time step for the simulation given as

$$\Delta t = \frac{1}{2f_c} \tag{4.4}$$

where f_c is the cut of frequency in hertz. This gives the following equation to determine number of points for a 10 minute simulation with $f_c = 2\,\text{Hz}$:

$$N = \frac{T}{2\Delta t} = \frac{600}{2 \times 0.25} = 1200 \tag{4.5}$$

So the cut of frequency, f_c, is set to $f_c = 2\,\text{Hz}$ and the number of frequency points, N, is set to $N = 1200$.

4.1.4 Exposure category

This simulation is based on the American standard ASCE 7-98, and preforms mean wind calculation based on the exposures categories found in this standard. Since the terrain below the bridge is a bit non-uniform, see figure 4.1, probably no exposure category may be set as a correct one. But assuming the exposures categories are the same in ASCE 7-98 and ASCE 7-05, exposure category C seems to be the most correct in this case. This is what ASCE 7-05 says about exposure category C [10]:

Exposure C: Exposure C shall apply for all cases where Exposures B or D do not apply.

Where exposure D and B is given as:

Exposure D: Exposure D shall apply where the ground surface roughness, as defined by Surface Roughness D, prevails in the upwind direction for a distance greater than 5,000 ft (1,524 m) or 20 times the building height, whichever is greater. Exposure D shall extend into downwind areas of Surface Roughness B or C for a distance of 600 ft (200 m) or 20 times the height of the building, whichever is greater.

Exposure B: Exposure B shall apply where the ground surface roughness condition, as defined by Surface Roughness B, prevails in the upwind direction for a distance of at least 2,600 ft (792 m) or 20 times the height of the building, whichever is greater.

Where Surface Roughness B, C and D is defined as [10]:

Surface Roughness B: Urban and suburban areas, wooded ares, or other terrain with numerous closely spaced obstructions having the size of a single-family dwellings or larger.

Surface Roughness C: Open terrain with scattered obstructions having heights generally less than 30 ft (9.1 m). This category includes flat open country, grassland, and all water surfaces in hurricane prone regions.

Surface Roughness D: Flat, unobstructed areas and water surfaces outside hurricane prone regions. This category includes smooth mud flats, salt flats, and unbroken ice.

The reason to use exposure category C is that the lowest modes of the bridge is manly constrained between pier 5 and 8 (see figure 4.1), and the surface under

this section of the bridge varies from flat sea approximately 60 m below the bridge to forested rocky slopes rising up towards the bridge to a height of 16 m below the bridge. But to check if the assumption that category C is the best suited for this case simulations with different exposure categories are to be preformed and compared.

4.1.5   Horizontal and vertical coordinates of simulated points

The NatHaz simulator [2] require x and z coordinates of up to 100 points when using the Schur decomposition by AR model and polynomial approximation. To get the best use out of these points the first eigenmodes of the bridge was studied, since the loading due to wind is most likely to excite the bridge at the first few natural frequencies. Almost all the movement of the first few modes are concentrated between pier 5 and pier 8 (see figure 4.1) so all the nodes are located between these two piers.

The wind velocity varies a lot with the height above ground, see eq. 2.4 and eq. 2.7, but not so much due to the horizontal distance between points, so since the arch varies more with height than the bridge deck it was chosen to place more points on the arch. So the simulations are run with 59 points one the arch and 41 on the bridge deck. The points on the arch then have an average separation between to adjacent points of 4.8 m along the arc length, while the points on the superstructure have an average horizontal separation of 8.25 m.

The NOWS seems to assume that the points are to be located above a flat surface so the z-coordinate seems to be used both to define a points height over ground and to define the distance between points. This could pose as a problem when used on the Svinesund bridge since the surface under the bridge is far from flat. It varies from flat sea approximately 60 m below the bridge to forested rocky slopes rising up towards the bridge to a height of 16 meters below one of the box girders (see figure 4.1) . To account for this four different approaches to specify the z-coordinates of the selected points are to be compared to see what gives the most accurate result. The four approaches are as follows:

z_1 Calculating an approximate real height under each point by approximating the surface to rise linearly between the sea and the arch abutments, and between each arch abutment and pier 5 and 8. The only exception to this is that the arch abutment on the Norwegian side (point 7A in figure 4.1) is blasted 7.437 m into the ground, so the linear rise here is from a point 7.437 m above the arc abutment and up to the

abutment of pier 8. This approach would give more emphasis on getting the height correct and assume that this is more important than the correlation effects between the points, thus probably making this the most accurate simulation with respect to the mean wind velocity.

z_2 Assuming the entire span between pier 5 and 8 lies over water. This would give correct correlation effects between points, but would give a bad representation of the height, particularly near pier 5 and 8, thus especially affecting the mean wind calculations.

z_3 A more conservative estimate than assuming the entire bridge lies over water would be to assume that the terrain under the bridge is uniformly distributed equal to the mean height of the terrain and the water surface, which is calculated to be 12.87 m.

z_4 The last approach is to set all the points over water to their correct value and to assume that the terrain has an equal height above the sea set to the mean value of the terrain height (24.10 m), and that this height is constant from the waterline and to pier 5 and 8. So the terrain is set to be constant of an height of 24.10 m above the waterline. This would be a sort of combinations between all of the approaches above, where the points to some degree have the correct height and to some degree have the correct separation between each other.

In Appendix A tables giving information about the points selected is given. Her one could find information such as the cross section where the node is located, the desired x-value found from calculation, the coordinates in the FE-model, the node number in the FE-model for both windward and leeward box girder, the length between to adjacent points, and the x-value and the four z-values used in the simulations.

4.2 Applying the simulated velocities on to the FE-Model

To apply the simulated wind velocities on to the FE-model, they first have to be transformed into force components. Since the wind velocities evaluated in this thesis seem to be somewhat strong wind velocities, but not extreme, the buffeting theory will be used to calculate the wind load. The buffeting load on structures includes the part of the total load that may be ascribed to the velocity fluctuations

in the oncoming flow as well as any motion induced contributions. The basic assumption behind the buffeting theory is that the load may be calculated from the instantaneous velocity pressure and the appropriate load coefficients that have been obtained from static test, and that linearization of any fluctuating parts will render results with sufficient accuracy. So the load may be calculated from an interpretation of the instantaneous relative velocity vector and the corresponding flow incidence dependent drag, lift and moment coefficients that are usually applied to calculate mean static load effects.

Since NOWS only gives the horizontal wind velocity perpendicular to the bridge, only horizontal accelerations will be investigated. So from this point on the only force considered would be the drag force.

The buffeting drag force are referred to the share center of a cross section and could be split into a mean and a fluctuating part, i.e.

$$\bar{q} = \frac{1}{2}\rho U^2(z)\, C_D A \tag{4.6a}$$

$$q = \frac{1}{2}\rho u(x,y,z,t)\, U(z)\, C_D A \tag{4.6b}$$

where ρ is the air density, set to $\rho = 1.225\,\mathrm{kg/m^3}$, which is the default value for air at sea level at $15\,^{\circ}\mathrm{C}$, C_D is the drag coefficient, A is the tributary area, $U(z)$ is the mean wind velocity and $u(x,y,z,t)$ is the fluctuating wind speed.

The fluctuating wind speed and the mean wind velocity are obtained from the simulation, so the only parameters left to find is the drag coefficient, C_D, and the tributary area, A.

4.2.1   Drag coefficients

4.2.1.1   Arch

In Simiu and Miyata [13] drag coefficients for several rectangular cross section are given. The arch sections width vs. height ratio varies from $B/D = 1.76$ at the abutments to $B/D = 1.48$ at the crown. For a rectangular cross section with $B/D \leq 2.0$ it is, in Simiu and Miyata [13], suggested to use a drag coefficient of $C_D = 0.8$ if one assumes that the onflow angel α is very small or equal to 0.

4.2.1.2   Superstructure

When it comes to the drag coefficient of the superstructure several wind tunnel tests were preformed before one arrive at the chosen design. The final report on

Table 4.3: Height for each arch section

Arch section	1	2	3	4	5
Height, D [m]	4.2	3.4	3.167	2.934	2.7

the chosen design [6] set the drag coefficient of both the steel box girders connected together as $C_D = 0.15$. For each box girder separate the drag coefficients are 0.08 for the windward girder and 0.06 for the leeward girder. All of these drag coefficients are taken for an onflow angel of $\alpha = 0$.

In Appendix B two plots of the drag coefficient versus onflow angle α from the wind tunnel test [6] is given along with figures showing the defined positive directions for Lift, Drag and Moment for two different onflow angles.

4.2.2 Tributary area

The tributary area used in eq. 4.6a and 4.6b depends on the chosen normalization used when calculating the drag coefficients, and may wary from test to test. Here it consists of half of the length between the two adjacent points to any given point, $L_{seperation}$, and a chosen normalization measurement. $L_{seperation}$ for each point in the simulation may be found in table A.2. The mean length of $L_{seperation}$ should be 4.8 m for points along the arch and 8.25 m for points on the superstructure.

4.2.2.1 Arch

The chosen normalization measurement for the arch is the height of the cross section. This means that the tributary area for the arch is the height multiplied with the separation of the adjacent points in the FE-model, $A = D \times L_{seperation}$. The height, D, of the arch varies from section to section as given in table 4.3.

A overview of which section each point lies within is given in table A.1. It is note taken into consideration that a point lying near the edge of a section could have different heights inside its length interval since this would not make such a large difference in the final results but make the calculation a bit more complex. So the time vs. gain factor was deemed to be to small for this to be implemented.

4.2.2.2 Superstructure

The chosen normalization measurement for the drag coefficient of the superstructure in the wind tunnel tests were the width of the entire cross section ($B = 27.60$ m in full scale).

The tributary area of the superstructure then becomes the width of the entire

cross section multiplied with the separation of the adjacent points in the FE-model, $A = B \times L_{seperation}$.

4.2.3   Strategies for applying the load

The load were applied to the FEM by the use of the CLOAD and AMPLITUDE keywords in Abaqus, with the help of input files generated in Matlab.

When applying the load on to the superstructure different strategies were used to see which strategy would give the most correct behavior. The different strategies are outlined below. For the four first strategies the loading on the arch were calculated with drag coefficient of $C_D = 0.8$. The results from the various strategies will be discussed in chapter 5.

1 point: Using the drag coefficient for the entire cross section, $C_D = 0.15$, and applying the full load only to the windward box girder.

Full in 2 points: Using the drag coefficient for the entire cross section, $C_D = 0.15$, and applying the full load to each box girder.

Half in 2 points: Using the drag coefficient for the entire cross section, $C_D = 0.15$, and applying half of the load to each box girder.

Full in 2 points separate C_D: Using the drag coefficient for each box girder separate, $C_D = 0.08$ for the windward box girder and $C_D = 0.06$ for the leeward box girder.

Full in 2 points $C_D = x, y, z$: Some tests to see if changing the drag coefficient of both the superstructure and the arch give a more correct results. Here x indicates the windward box girders C_D, y the leeward box girder and z the drag coefficient of the arch. If only two values are present the windward and leeward drag coefficient are the same.

Chapter 5

Results

In this chapter the results of the different simulations will be presented and discussed. To compare the results from the simulation with the ones from the measurements several different factors will be examined, including the mean and maximum wind velocity at the location of the anemometer, the standard deviation of the wind velocities, and the standard deviation of accelerations at given locations on the bridge. A spectral examination of the accelerations will also be preformed an compared. But first a brief explanation regarding the measurement of Svinesund bridge is presented.

5.1   Measurement of the Svinesund bridge

Since the Svinesund Bridge is such an unique structure being, at least at the moment it was built, the world's longest arch bridge with a single central arch an advanced measurement system was installed during the construction phase to monitor and check the that the bridge functions as intended during the this phase and the first years of operation. This system consists of many different sensors collecting information about wind speeds, accelerations, strains and temperatures to mention some. The sensors of interest in this project are 4 of the 10 accelerometers measuring accelerations in the horizontal direction perpendicular to the bridge, and a anemometer measuring the wind. For placement of the different measurements see table 5.1 and figure 5.1. A larger version of figure 5.1 is also reproduced as fig. Placement of sensors in Appendix C.

The accelerometer and the anemometer all have a sampling frequency of 50 Hz, and every 10 minute the maximum and minimum values as well the standard

Table 5.1: Placement of sensors

Name of sensor	Type of sensor	Location of sensor
ACCQ-YW	Linear Servo Accelerometer	1/4 point bridge, West side, Y-dir, (y = transverse)
ACCM-YW	"	1/2 point bridge, West side, Y-dir
ACCS14-Y	"	S14 arch, Y-dir
ACCN26-Y	"	N26, Top arch, Y-dir

Winddir	3-Axis Ultrasonic Anemometer	Beside pier 5 (Bjälvarpet), wind direction
WindH	"	Beside pier 5 (Bjälvarpet), horizontal wind speed
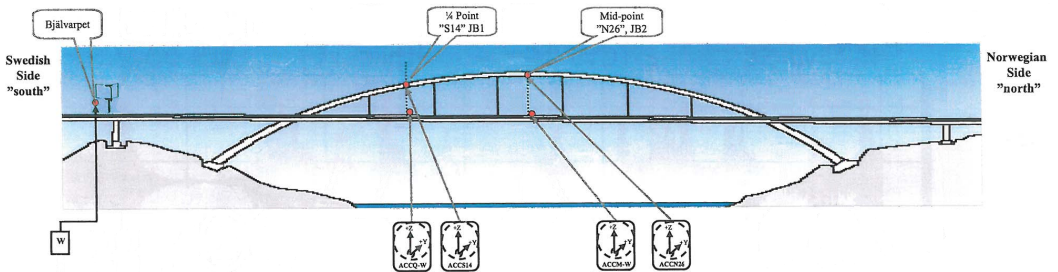
Figure 5.1: Placement of sensors

deviation are calculated and stored, along with the time the at which the values were registered. After each 10-minute interval the storage buffer of the measurement system is full and all the raw data is overwritten. But if the wind speed or the bridge vibration (acceleration) exceeds a predetermined limit value, the raw data for the entire 10-minute interval are saved. The measurements used in this thesis is collected from 90 such 10-minutes intervals taken as the storm Per passed the Svinesund Bridge January 14, 2007. Out of these 90 series some are more interesting than the others, and in this chapter a closer look would be given to the 58th 10-minute interval, which is the series that has the largest 10-minute-mean velocity, $\overline{U}_{10} = 23.03\,\mathrm{m/s}$. The 57th and 59th series are also examined too see if more raw data makes any difference on the results.
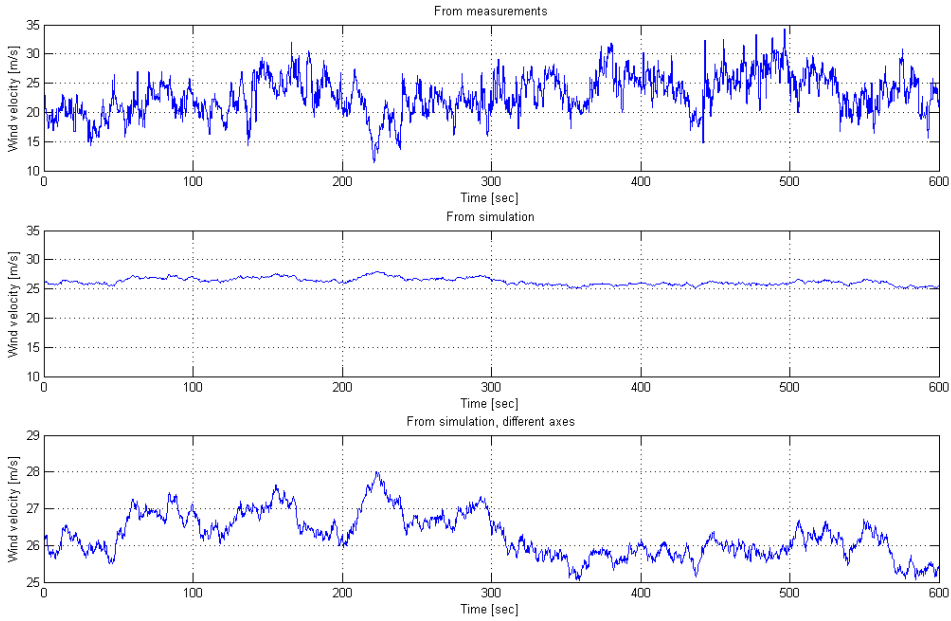
Figure 5.2: Plot of wind velocities for measurement interval 58 and simulation with exposure category C and the z_1 approach. Notice the difference in the x-scale for the last plot.

5.2 Comparison of wind velocities

A plot of the wind velocity from interval 58, which is the series that has the largest 10-minute-mean velocity, $\overline{U}_{10} = 23.03\,\mathrm{m/s}$, and a simulated wind velocity at simulation point number 60 (located at the same location as the anemometer) with exposure category C and the z_1 approach (explained in section 4.1.5) is given in figure 5.2. In this figure one could see that the fluctuation in the simulated wind velocity is much lower than the fluctuation in the measured wind.

Figure 5.3 and 5.4 shows the wind velocity from different simulations. In fig. 5.3 the different simulation approaches z_n ($n = 1, 2, 3, 4$) are compared against each other, while fig. 5.4 shows how changing the exposure category affects the wind velocities. From these figures it seems that z_1 has the lowest mean wind velocity, as expected since the height at the anemometer is lowest using the z_1 approach. It also seems that changing the exposure category changes both the mean value of the velocity and the turbulence in the wind field, both increasing when going from exposure category A to category D. This first is explained by the fact that changing exposure category changes both the roughness length z_0 and the terrain
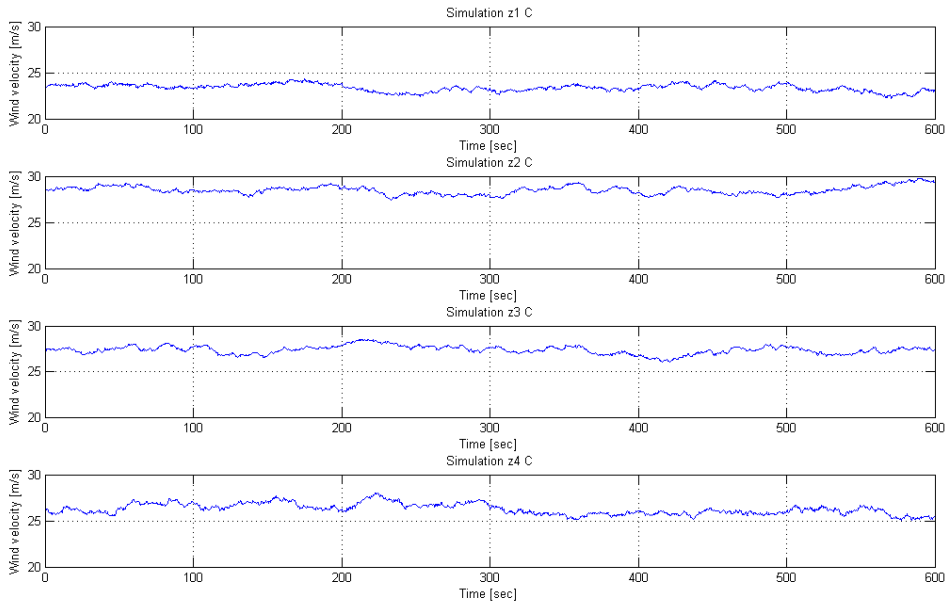
Figure 5.3: Plot of wind velocities for the different simulation approaches z_1 to z_4.

factor k_T, and this in turns affects the mean wind velocity as given in eq. 2.4. So the expected effect of going from the flat an smooth terrain D with high $U(z)$ to the rough an coarse terrain A with low $U(z)$ is found in the simulations. The reason the turbulence increases going from exposure category A to D is not so obvious. One should think that a rougher terrain creates more turbulence since the shear friction increases with roughness. But going from a terrain with exposure category D to a terrain with exposure category A also means that the obstructions near ground gets larger and higher, thus lifting the threshold for where the turbulence is strong higher into the air (higher zone near ground with high shear friction would lower both the mean wind velocity and the turbulence in this band, thus increasing the height were the turbulence could become sufficient large). This might explain the reason that exposure category D has the highest standard deviation at the anemometer (17 m above ground). There are also some random variations between the simulations that could explain some of this difference.

The different maximum and mean values and the standard deviation of the wind velocities at the the anemometer (Point number 60 in table Appendix A, i.e. FEM node number 20), see fig. Placement of sensors, fig. Placement of sensors, is given in table Wind velocities. An explanation to this table is as follows
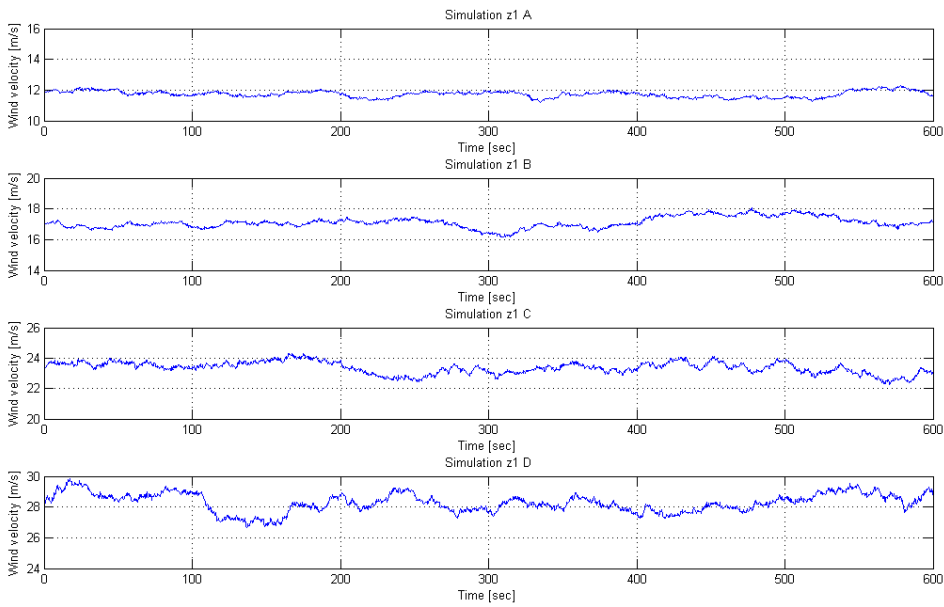
Figure 5.4: Plot of wind velocities from simulations using different exposure category A to D. Important to notice that the values of the x-axis changes, but not the scale.

$Max(U)$ Indicates the maximum velocity

$Mean(U)$ Indicates the mean velocity

$Std(U)$ Indicates the standard deviation of the velocities

Mean all   Calculation based on the mean values calculated from each of the 90 10-minute intervals. So in this row the max and mean value of all the 90 10-minute-mean-values, and the mean value of the standard deviation of each of the 90 series are given.

Series 58   Calculation based on values from the 58th 10-minute interval which is the series that has the largest 10-minute-mean velocity, $\overline{U}_{10} = 23.03\,\mathrm{m/s}$. So in this row the max value recorded in the 58th interval, the mean value of the recorded velocities in the 58th interval, and the standard deviation of all the recorded velocities the 58th interval is given.

Series 57 to 59 Calculation based on values from the 57th, 58th and 59th interval. This would then give the max value recorded in any of these three intervals, the mean value of the recorded velocities in these three intervals

Table 5.2: Wind velocities

		$Max(U)$	$Mean(U)$	$Std(U)$
	Mean all	23.03	11.85	2.84
From measurements	Series 58	34.32	23.03	3.42
	Series 57 to 59	34.32	21.31	3.51
	z_1, C	24.29	23.36	0.39
	z_2, C	29.80	28.49	0.44
	z_3, C	28.59	27.36	0.45
From simulations	z_4, C	28.02	26.27	0.59
	z_1, D	29.85	28.29	0.61
	z_1, B	18.04	17.12	0.36
	z_1, A	12.31	11.74	0.21

combined, and the standard deviation of all the recorded velocities in these three intervals.

z_n, X   Means that this is data from the simulation that used the n-th z-value approach ($n = 1, \ldots, 4$) and has exposure category X (X = A, B, C, D).

Table Wind velocities shows that the z_1 simulation gives the best prediction of the mean wind velocity, as suggested in section 4.1.5. It could also be seen that the simulated wind velocities have a much smaller standard deviation than the measured ones (all of the 90 10-minute intervals had a standard deviation above 2), indicating that the simulation is a bit too conservative when it comes to creating turbulence in the wind field. This is also clearly seen in fig. 5.2. The table also shows that the prediction made based on fig. 5.4 that both the mean velocity and turbulence in the wind field is increasing when going from exposure category category A to category D. The standard deviation from the simulations shows an apparent trend of becoming larger as one goes from exposure category A to exposure category D, D having three times the standard deviation of A.

5.3   Comparison of acceleration

Figure 5.5 and fig. 5.6 shows the acceleration at node 511 on the superstructure and node 422 on the arch (located at the mid point of the arch and the superstructure), respectively, demonstrating the difference between the measured accelerations and the acceleration from simulations with exposure category C and the z_1 approach. These figures shows a trend were the simulated accelerations seems to have lower amplitude than the measured acceleration.
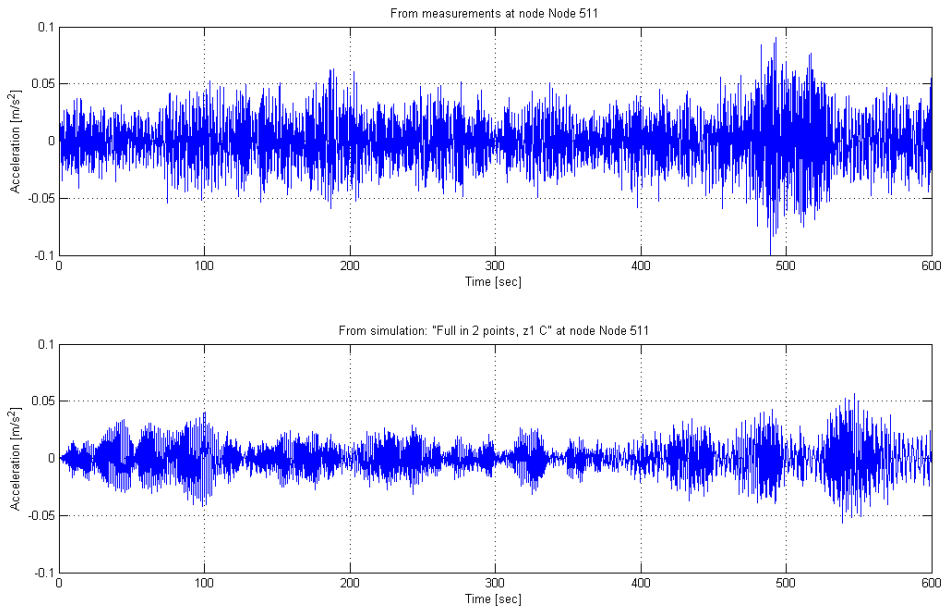
Figure 5.5: Acceleration at node 511 from measurements and simulation *Full in 2 points* using exposure category C and the z_1 approach.
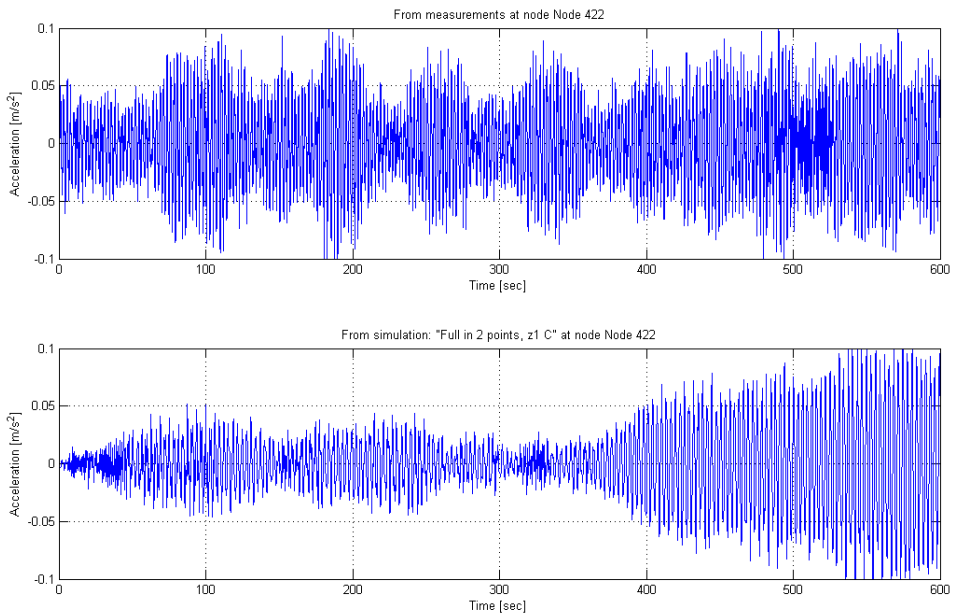
Figure 5.6: Acceleration at node 422 from measurements and simulation *Full in 2 points* using exposure category C and the z_1 approach.
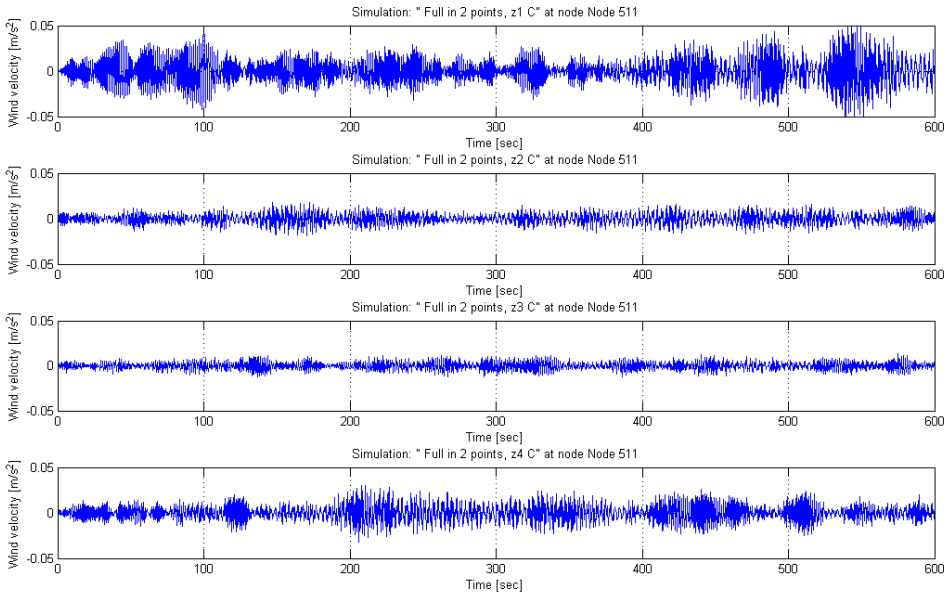
Figure 5.7: Plot of acceleration at node 511 from simulation *Full in 2 points* using exposure category C and varying simulation approach from z_1 to z_4.

Figure 5.7 shows how the acceleration at node 511 (mid point of bridge) changes when varying the simulation approach from z_1 to z_4. Here one could see that z_1 seems to have more fluctuations than the others, especially more than z_3. This could be explained by the fact that the z_1 approach puts the nodes closer to ground, where the turbulence is higher than for the nodes in the z_3 approach, which are located somewhat higher. But this could also just be due to random variation within each simulation due tho the added noise in the simulation.

Figure 5.8 shows how the acceleration at node 511 (mid point of bridge) changes when varying the exposure category from A to D. Here one could see that there is not a very big difference when varying the exposure categories, but category A and B seems to have smaller amplitude, indicating less standard deviation, than category C and D. The reason for this is the same as the one discussed in section 5.2 on how changing the exposure category changes the wind velocity and the standard deviation of the wind velocities.

Figure 5.9 shows how the acceleration at node 511 (mid point of bridge) changes when varying the simulation strategy. Here one could see that there is a big difference between the *Full in 2 points* strategy from the others. This occurs because the load in this strategy is approximate double that of all the other strategies used.
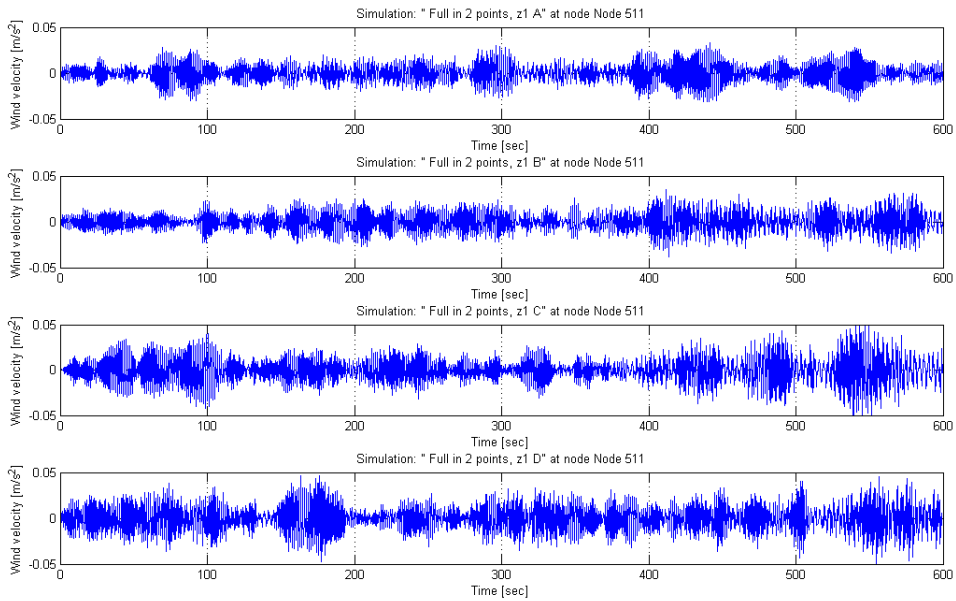
Figure 5.8: Plot of acceleration at node 511 from simulation *Full in 2 points* using simulation approach z_1 and varying the exposure category from A to D.

One could also notice that there are almost no difference if one uses the drag coefficients for each box girder separate (see section 4.2.1.2), applies half the load of the unified drag coefficient to each girder or applies the full load only on to the windward girder. This indicates that the measurements from the wind tunnel test seems to be good, since applying load to one or both girders with the different drag coefficients seems to give the same result. It also indicates that the superstructure is quite stiff, since there are almost no difference in applying the full load to one girder, applying half the load to each girder or applying scaled loads to each girder. The load on the bridge seems to be almost the same. If this is indeed correct behavior or if this is an error in the FEM does not lie within the scope of this thesis to calculate.

The standard deviation of the acceleration at the location of the accelerometers are compared in table 5.3. Here the standard deviation is given for the measured acceleration, but for the simulations the difference between the standard deviation for the simulation and the standard deviation found in the measured accelerations of interval 58 are given, (for ex. $Value_{1point,z_1,c,152} = std(accel_{ACCQ-YW(Node\,152)}) - std(accel_{1point,z_1,c,152}))$. An explanation to the table is given below:
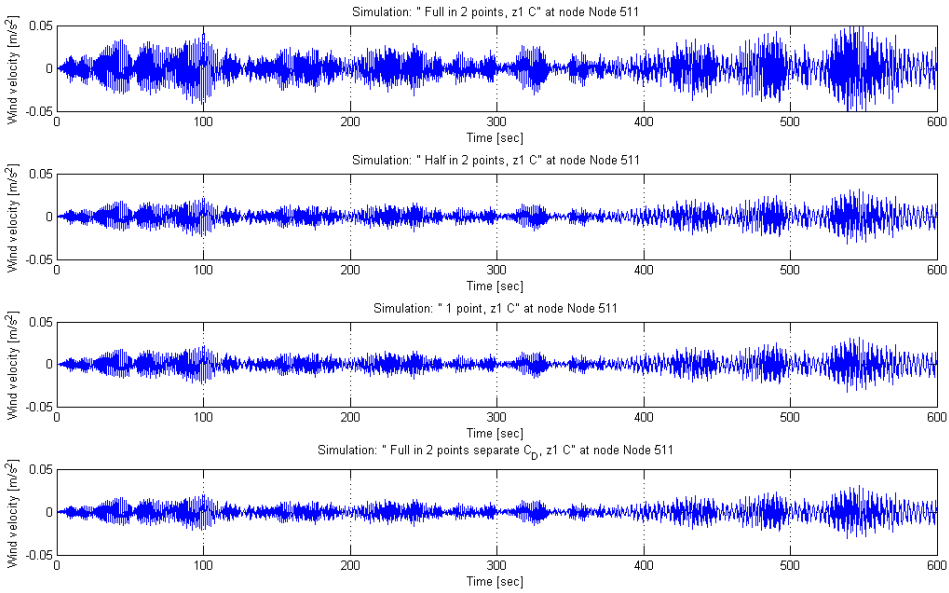
Figure 5.9: Plot of acceleration at node 511 using simulation approach z_1, exposure category C and varying the simulation strategy between (top-down) *Full in 2 points*, *Half in 2 points, 1 point* and *Full in 2 points separate* C_D.

Mean: Calculation based on the mean value from each of the 90 10-minute intervals, so the value given here is the mean value of the standard deviation from each of the 90 series.

Max: Calculation based on the mean value from each of the 90 10-minute intervals, so the value given here is the max value of the standard deviation of each of the 90 series.

58:         Calculation based on values from the 58th interval which is the series that has the largest 10-minute-mean velocity, $\overline{U}_{10} = 23.03\,\mathrm{m/s}$.

1 point: Calculation based on simulation using the drag coefficient for the entire cross section, $C_D = 0.15$, and applying the full load only to the windward box girder.

Full in 2 points: Calculation based on simulation using the drag coefficient for the entire cross section, $C_D = 0.15$, and applying the full load to both box girders.

Half in 2 points: Calculation based on simulation using drag coefficient for the entire cross section, $C_D = 0.15$, and applying half of the load to each box girder.

Full in 2 points separate C_D: Calculation based on simulation using the drag coefficient for each box girder separate, $C_D = 0.08$ for the windward box girder and $C_D = 0.06$ for the leeward box girder.

Full in 2 points $C_D = x, y, z$: Calculation based on test simulations made to see if changing the drag coefficient of both the superstructure and the arch give a more correct results. Here x indicates the windward box girders C_D, y the leeward box girder and z the drag coefficient of the arch. If only two values are present the windward and leeward drag coefficient are the same.

Node 152: Node number 152 which equals accelerometer ACCQ-YW, and is located at the 1/4 point of the superstructure within the arch section.

Node 272: Node number 272 which is the node located on the east box girder at the 1/4 point of the superstructure within the arch section, opposite to Node 152.

Node 511: Node number 511 which equals accelerometer ACCM-YW, and is located at the mid point of the superstructure within the arch section.

Node 661: Node number 661 which is the node located on the east box girder at the mid point of the bridge (opposite to Node 511).

Node 872: Node number 872 which equals accelerometer ACCS14-Y, and is located on the arch at the horizontal 1/4 point of the arch, above node 152 and node 272.

Node 422: Node number 422 which equals accelerometer ACCN26-Y, and is located at the mid point of the arch, above node 511 and node 661.

z_n, X: Means that this is data from the simulation that used the n-th z-value approach ($n = 1, \ldots, 4$) and has exposure category X (X = A, B, C, D).

Table 5.3 shows in numbers what was indicated in fig. 5.7, namely that the z_1 simulation gives the best results if one looks at the standard deviation of the accelerations, just as it gave the most correct simulation when looking at the wind

Table 5.3: Comparison of standard deviation of acceleration between the simulated results and the values from the 58th 10 minute interval, containing the largest 10 minute mean velocity, $\overline{U}_{10} = 23.03\,\mathrm{m/s}$

		Node 152	Node 272	Node 511	Node 661	Node 872	Node 422
From measurements	Mean	0.0055	-	0.0071		0.0077	0.0120
	Max	0.0177	-	0.0231	-	0.0276	0.0406
	58	0.0150	-	0.0193	-	0.0238	0.0368
1 point	z_1, C	0.0083	-	0.0110		0.0082	0.0115
Full in 2 points	z_1, C	0.0032	0.0032	0.0044	0.0044	0.0031	0.0026
	z_2, C	0.0099	0.0099	0.0134	0.0134	0.0096	0.0147
	z_3, C	0.0113	0.0113	0.0150	0.0150	0.0163	0.0265
	z_4, C	0.0076	0.0076	0.0102	0.0102	0.0067	0.0093
Full in 2 points	z_1, D	0.0025	0.0025	0.0040	0.0040	0.0052	0.0061
	z_1, B	0.0060	0.0060	0.0081	0.0081	0.0086	0.0117
	z_1, A	0.0064	0.0064	0.0085	0.0085	0.0133	0.0192
Half in 2 points	z_1, C	0.0083	0.0083	0.0110	0.0110	0.0082	0.0115
	z_4, C	0.0107	0.0107	0.0141	0.0141	0.0112	0.0166
Full in 2 points separate C_D	z_1, C	0.0086	0.0086	0.0115	0.0115	0.0086	0.0120
Full in 2 points $C_D = 0.15, 0.06, 0.8$	z_1, C	0.0063	0.0063	0.0084	0.0084	0.0062	0.0079

velocity. The table also shows that the *Full in 2 points* load strategy with $C_D = 0.18$ for both box girders gives the best result, but if this is correct will be discussed in chapter 6. The table also reveals what could be seen in fig. 5.9, that there are almost no difference between the three load strategies *Half in 2 points*, *1 point* and *Full in 2 points separate* C_D. When it comes to exposure categories table 5.3 reveals that the indication in fig. 5.8 indicating less standard deviation in category A and B than category C and D is correct. It is also noted that category C and D both gives reasonable correct simulations, and there have not been conducted enough comparisons between simulations and measurements in this thesis to say that one is more correct than the other. But doing so do not lie within the scope of this thesis either.

To check if the 58th interval contains unusual turbulence distribution, and if it might be more correct to include the 57th and the 59th 10-minute interval as well as the 58th in a comparison with the simulated results another table (table

Table 5.4: Comparison of standard deviation of acceleration between the simulated results and the values from the 57th , 58th and the 59th 10 minute interval.

		Node 152	Node 511	Node 872	Node 422
Measurements	57 to 59	0.0136	0.0175	0.0209	0.0311
Full in 2 points	z_1, C	0.0018	0.0026	0.0001	-0.0032
	z_4, C	0.0062	0.0084	0.0037	0.0035
	z_1, D	0.0011	0.0022	0.0022	0.0004

5.4) is presented. In this table the standard deviation for the simulated results are compared to all the three 10-minute intervals mentioned, and the values given are the difference between the simulated results and the ones measured from the 57th, 58th and the 59th 10-minute intervals put together. In table 5.4 node 272 and node 661 were omitted because they give the exact same result as node 152 and 511 respectively, as seen in table 5.3. All the explanations given for table 5.3 remains valid for table 5.3 with addition of:

57 to 59:   Calculation based on values from the 57th, 58th and 59th 10-minute interval.

In this table it may be observed that the simulated values corresponds much better with the measured ones when more values are taken into consideration. Especially the simulation with exposure category D are very accurate for node 152 and 422, and the simulation with exposure category C is almost spot on at node 872, giving almost no difference in the standard deviation of the accelerations. This may indicate that the 58 interval contains a very turbulent wind field, and therefore do not correlate as well with the simulations, since they are more moderate in their turbulence content.

5.4 Spectral analysis

The spectral analysis conducted in this thesis is based on the Burg method of obtaining the power spectral density function (PSD). The PSD describes how the power of a time series is distributed with frequency. In other words it shows at which frequencies variations of a time series are strong, by *peaks* appearing in the PSD, and at which frequencies variations are weak.

A short description of the Burg method for estimating the PSD is given below. For a more thorough review see Fiskum [5].

Burg method   The Burg method of PSD estimation is conducted by fitting an AR
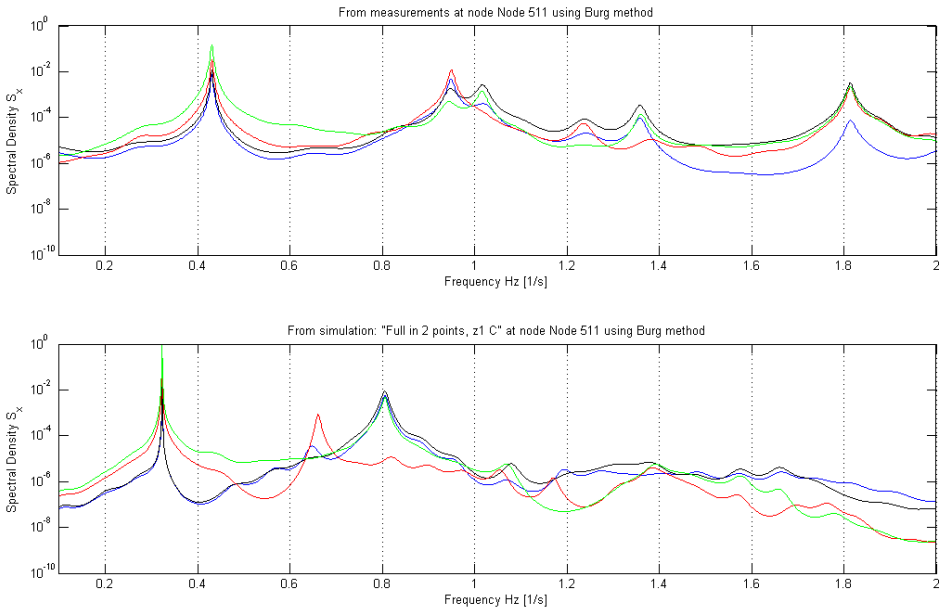
Figure 5.10: PSD from measured accelerations at node 511 from the 58th 10 minute interval compared to the PSD from simulated accelerations using simulation strategy *Full in 2 points*, exposure category C, and the z_1 approach.

linear prediction filter model of a specified order to the input signal by minimizing the arithmetic mean of the forward and backward prediction errors. The spectral density is then computed from the frequency response of the prediction filter.

5.4.1   Spectral analysis of accelerations

In figure 5.10 one could see the the PSD from the acceleration measured at node 511 in the 58th 10-minute interval compared with the PSD from the simulated accelerations in the same point with simulation strategy *Full in 2 points*, simulation approach z_1 and exposure category C. Here the measured response have peaks at 0.45 Hz, 0.95 Hz, 1.0 Hz, 1.25 Hz, 1.35 Hz and 1.80 Hz while the simulated response have peaks at 0.30 Hz, 0.65 Hz and 0.8 Hz. The reason the simulated response seems to roll of when it approaches 2 Hz is that it then approaches the cut off frequency ($f_s = 2$ Hz), also called the Nyquist frequency. Beyond this frequency no useful information is collected.

Figure 5.11 and 5.13 shows that neither changing the simulation approach (i.e. how the height of the points are represented), varying the exposure category from A
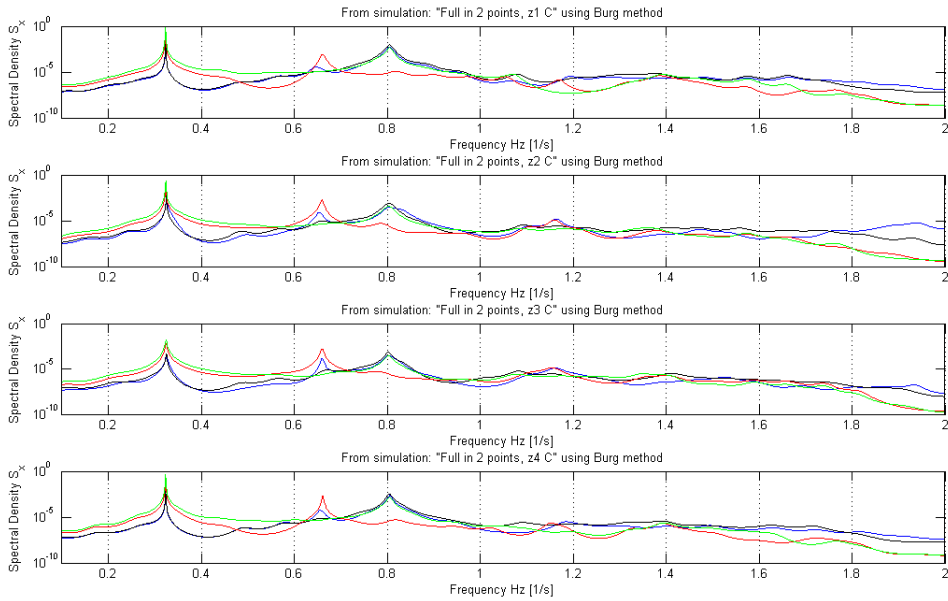
Figure 5.11: PSD from simulated accelerations with simulation *Full in 2 points* using exposure category C and varying simulation approach from z_1 to z_4.

to D nor using different simulation strategies affect the PSD matrix of the simulated accelerations, indicating that the frequency content of the wind is maintained no matter which load strategy, exposure category or z-approach one chooses. At least for the last property this seems to be an wanted effect, since varying the intensity of the load do not change the frequency spectrum of the response. The only way this would happen is if the load is so strong that it either changes the structural stiffness or the structural damping of the system. But that changing the exposure category or the height and separation between points have almost no effect on the frequency response is strange seems strange since both these factor should change how the PSD matrix on which the time series simulation is based should also change the frequency content of that simulated time series.
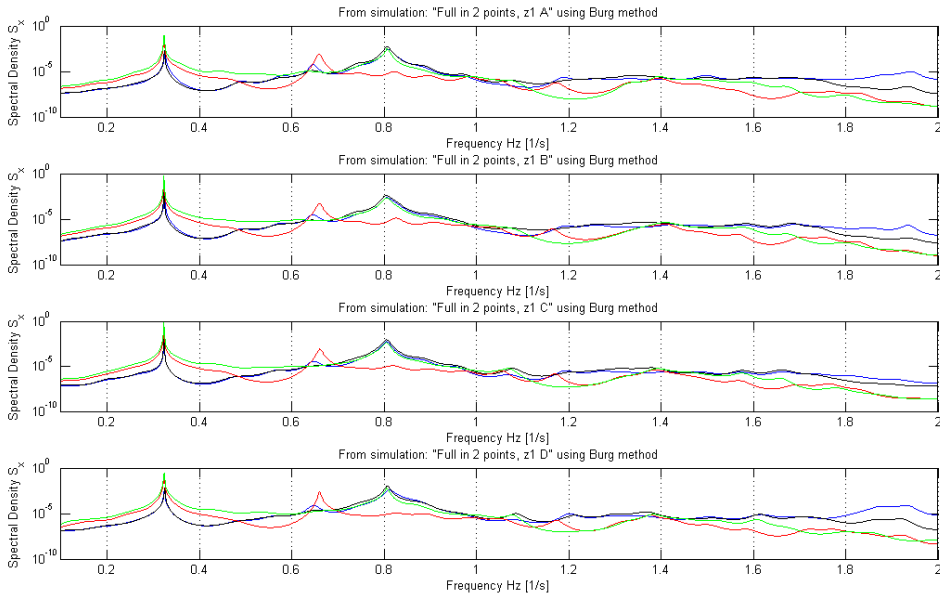
Figure 5.12: PSD from simulated accelerations with simulation *Full in 2 points* using simulation approach z_1 and varying the exposure category from A to D.
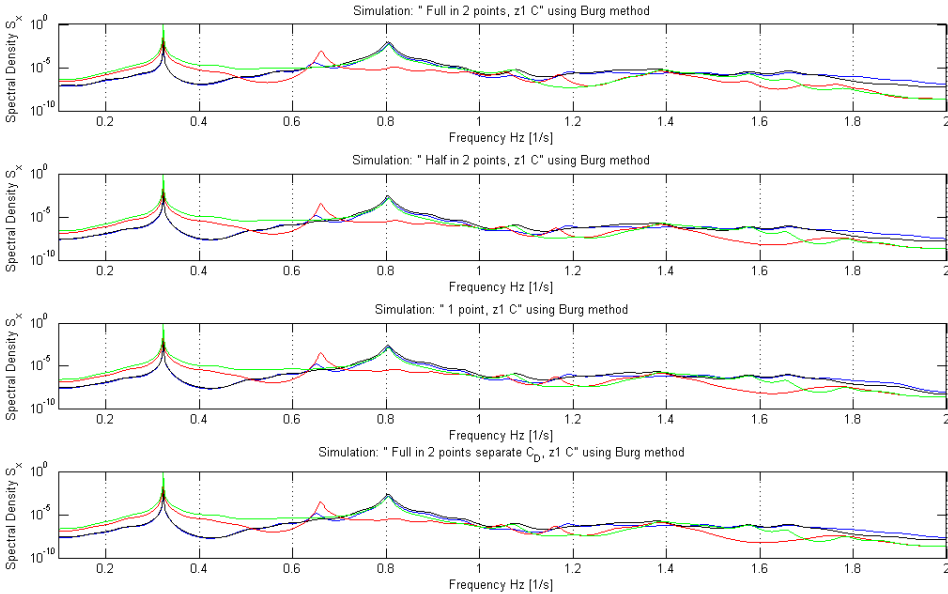
Figure 5.13: PSD from simulated accelerations using simulation approach z_1, exposure category C and varying the simulation strategy between (top-down) *Full in 2 points*, *Half in 2 points*, *1 point* and *Full in 2 points separate* C_D.

Chapter 6

Sources of error and possible improvements

This chapter presents a discussion around sources of error and possible improvements, with further studies within this topic or work based on this thesis in mind.

6.1   Error in the finite element model

In Fiskum [5] many of sources for errors were discussed in terms of the FEM model. No further investigations into those suggested there was made to correct the model in this thesis. It was rather decided to spend time getting a deeper understanding of time domain simulation of wind velocities. But to repeat some of the most important sources of errors found by Fiskum [5] the largest uncertainty lies in the determination of the modulus of elasticity for the concrete arch. Especially whether to assume that it has cracked or not. This greatly affect the FEM since changing this value to a large degree affects the entire stiffness of the bridge. Another uncertainty that may be wise to investigate further is the connection between the piers and the superstructure, and what impact the fact that the cross beams being clamped to the piers by 8 tendons have on the connection. It is also recommended to take a closer look at the abutment of pier 4, since this is resting on soil supported by 26 steel-core piles. The last refinement suggested worth looking into is to refine the non-linear geometries of the arch and the pillars by dividing them up into smaller segments. Especially refining the arch could have some impact on the results.

An error that has arrived in this thesis is the fact that the element size of the

mesh was increased from 1 m to 5 m. This was done to shorten the simulation time when calculating response from the 10 minute long simulation. Reducing the number of nodes was vital to become capable of calculating the response within a reasonable time.

6.2   Error in the time series simulation

Since some time of this thesis was lost in the investigation of what turned out to be a dead end, time constraints led to the use of the NatHaz On-line Wind Simulator (NOWS) instead of writing a new simulation. This means a loss of control over what happens during the generation of the simulations, and even though a brief theoretical background and references to the theory used in the development of the NOWS were given, the actual code has never been investigated in this thesis. This makes it difficult to know whether any errors occurs in the generation of any of the simulations. But since such an approach was necessary due to time constraints, a thorough examination of the theory behind the simulations was preformed, and it appears to be based on acknowledged models from the theory of wind engineering and numerical mathematics. So when it comes to errors that may occur during the generation of the time series, they are considered to be beyond what can be controlled in this thesis. If a further study of this subject is considered, one should consider whether it might be better to create a new simulation where one have complete control over all the input parameters and the calcuations preformed.

6.3   Errors in the input to the NatHaz On-line Wind Simulator

When using NOWS several inputs are required. Among these there might be room for errors.

6.3.1   Error in the choice of nodes

The selection of which points the wind simulations were to be performed in were done on the basis of a number of considerations such as how the bridge would behave under the wind load, how to best represent the variation in geometry and how to obtain the best correlation between simulated and measured values. And the chosen solution may be far from providing the best possible solution. But based on the results the chosen solution seems to be adequate.

6.3.2 Errors in the selected approaches of z-coordinates

In this thesis four different approaches to specify the z-coordinates were tested. The one that turned out to be most accurate was the z_1-approach, where a real height is approximated using an assumed piecewise linear rise of the terrain. But whether this is the best solution available is far from certain, and many other approaches requires testing before any definitive conclusions can be drawn. Again, writing a new simulation, which can take variation of the terrain into account, could provide more bang for the buck than further testing of this solution.

6.3.3 Uncertainty in the validity of the 3-sec gust wind formula

No attempt has been made in this thesis in order to validate the 3-sec gusts formula, except to confirm the validity of it as it is represented in a well-known book on the subject.

6.3.4 Uncertainty in the choice of exposure category

To avoid this uncertainty all the exposure categories were examined. As expected, category A and B, were the ones who differed most from the measured values. Category C and D were both very accurate and several thorough tests needs to be conducted if one are to declare one more suitable than the other.

6.4 Errors when the load was applied to the element model

6.4.1 Error near the intersection of two arch section

It is not, in this thesis, taken into consideration that the intersection of two parts of the arch may be located within the tributary are of a node. To incorporate this correctly the tributary area should have been split into two parts both accounting for the height of the cross section in their part. The error in not doing this is deemed to be small and it is just as likely to be a conservative approach as a non-conservative approach.

6.4.2 Error in the in the different strategies for applying the loading onto the FEM

In this thesis several strategies for load appliance are used. The one that seems to correlate best with the result are the one called *Full in 2 points*. The physical

explanation of this load is that a drag coefficient of the entire superstructure, both girders combined, is used to calculate a force which is applied to both the windward and the leeward girder. This should produce a force that is too high, because if one wants to apply load onto both girders, separate drag coefficient for each girder is given (see Appendix B). But using this approach, which in this thesis is called *Full in 2 points separate* C_D, do not produce the most correct result compared to the measured values. All of the strategies used in this thesis also seems to create the same PSD function, indicating that the frequency content of the wind is maintained no matter which load strategy one chooses. So in this thesis it seems that the best strategy is the *Full in 2 points*.

6.5   Summation

In this chapter several errors what identified and some solutions on how to improve the the accuracy of the model are made. The two main improvements that could present a big performance boost in an later study would be to take a closer look at the modulus of elasticity for the concrete arch, figuring aout if any cracking of the concrete have, and thus calculating a more accurate modulus of elasticity. The other improwment would be to find a new simulation procedure were one could have better control on the input and calculation, either by writing ones one or by finding a simulation where the source code is known.

Chapter 7

Conclusion

In this thesis a theoretical study in the field of time–series simulation of wind induced dynamic load was presented. Starting with some basic theory concerning wind and wind-statistics before moving on to an explanation of time-domain simulation of wind, with emphasis on the Schur decomposition by AR model and polynomial approximation, explained more thorough in the papers by Di Paola [11] and Di Paola & Gullo [12]. This is a method where the the goal is to simulate a *n-variate one-dimensional* (*n*-V, 1-D) stochastic vector process $\mathbf{V}(t)$, containing wind field velocities from n points in space. This is done by a summation of independent fully coherent stochastic processes as follows

$$\mathbf{V}(t) = \sum_{k=1}^{n} \int_{-\infty}^{\infty} \mathbf{q}_k(\omega)\, e^{i\omega t} \mathrm{d}B_k(\omega)$$

The advantages of the Schur decomposition by AR model and polynomial approximation approach to time domain solution lies in the decomposition of the PSD matrix $\mathbf{S}$ into the basis of the eigenvectors. The advantage being that very few spectral modes exhibit significant power, meaning that one could truncate the spectral modal matrix to a summation of only the modes having significant power, say m ($m \ll n$), only evaluating the m first eigenvectors. Another advantages is that each component of the eigenvectors is a relative regular function such that using iterative methods for evaluating eigenvalues and eigenvectors, and using the eigenvectors at the previous frequency ω_{k-1} as a first attempt, very few iterations are required in order to compute eigenvalues and eigenvectors at the current frequency ω_k. This is then taken advantage of when the the eigenvector is approximated

in a generic interval in a polynomial form of fixed order (third order polynomial
used in the text and later in the simulator). One is then able to approximate the
eigenvectors by generating $(4 \times M)$ independent univariate processes, instead of an
n-variate vector process. It is then shown how these $(4 \times M)$ independent univariate
processes could be generated using the standard generation via AR model. In the
end a description is given of how one could compute the $\mathbf{V}(t)$ from these generated
$(4 \times M)$ independent univariate processes.

Another advantage of this model discussed in the theoretical study is the phys-
ical meaning of eigenvectors and eigenvalues of the matrix $\mathbf{S}(\omega)$, where the eigen-
values are the power of the two independent processes $W_1(t)$ and $W_2(t)$, while
the eigenvectors are the mode shapes associated with the wind field velocity. It is
explained how the bivariate wind field blows as a sum of two independent totally
coherent processes associated with blowing shapes just as a structural vibration
is decomposed as a sum of independent structural mode shapes. This was also
visualized in fig. 3.2. It is then shown how this also is true for a six-variate wind
field.

Then the jump was made onto the creation of simulations of a wind field,
and how this thesis based its simulation on the NatHaz On-line Wind Simulator
(NOWS) [2]. Here a discussion were presented regarding different input to NOWS
as well as a discussion on how the simulated wind field velocities was to be applied
onto the FEM. In the end after looking at both the velocities and accelerations it
was concluded that the *Full in 2 points* simulation with approach z_1 made the best
representation of the measured response. *Full in 2 points* uses a drag coefficient of
$C_D = 0.15$ on both the windward and the leeward box girder, while the arch has
a drag coefficient of $C_D = 0.8$. The z_1 approach indicate that the z-coordinates
should be given as if the surface is raising linearly between the sea and the arch
abutments, and between each arch abutment and pier 5 and 8. It is also concluded
that the simulated response shows much lower values of variation compared to the
measured response.

At last in chapter 6 sources of error and possible improvements are discussed.
The last one with further studies within this topic or work based on this thesis in
mind. One of the topics raised here is the uncertainty in the FEM model, which
have not changes since Fiskum [5], other than the usage of a coarser mesh (element
size increased form 1 m to 5 m). So the errors discussed in Fiskum [5] also applies
here, and in Fiskum [5] the stiffness of the arch was especially noted for having

a large impact on the total stiffness of the bridge, but not thoroughly calculated neither in this thesis nor in Fiskum [5]. Another issue that was discussed was the problem in working with a black box, as done with the NOWS. Since none of the source code is known this creates issues such that one can not tweak any other factors than the one given through the online user interface, and one do not know exactly how the calculations are preformed.

So two improvements that could present a big performance boost in an later study in the same field would be a closer look at the modulus of elasticity for the concrete arch and to try and create a new simulation procedure were one could control both input and calculations at a larger degree, either by writing ones one or by finding an open sourced approach somewhere.

References

[1] NatHaz(Natural Hazards) Modeling Laboratory at the University of Notre Dame. Brief summary of nathaz on-line wind simulator's theoretical backgrounds. Visited in the period 01.03.12 to 11.06.12 at the adress: `http://windsim.ce.nd.edu/int_winsim.html`.

[2] NatHaz(Natural Hazards) Modeling Laboratory at the University of Notre Dame. Nathaz on-line wind simulator. Visited in the period 01.03.12 to 11.06.12 at the adress: `http://windsim.ce.nd.edu/doc/Theo_backg1.pdf`.

[3] T. Darholm, L. Lundh, R. Ronnebrant, R. Karoumi, and M. Blaschko. *Technical book about the Svinesund bridge*. Vägverket, December 2007.

[4] C. Dyrbye and S.O. Hansen. *Wind loads on structures*. J. Wiley, 1997.

[5] J. Fiskum. System identification of constructions - dynamic response of the svinesund bridge. Project report in the course TKT4511, NTNU, 2011.

[6] M. Hortmanns. *Global Structure, Wind Tunnel Tests, Final Report, 100K1503 Rev01*. Vägverket, 2003.

[7] J. C. Kaimal, J. C. Wyngaard, Y. Izumi, and O. R. Coté. Spectral characteristics of surface-layer turbulence. *Q.J.R. Meteorol. Soc.*, 98:563–589, 1972.

[8] Y. Li and A. Kareem. Simulation of multivariate random processes: Hybrid dft and digital filtering approach. *J. Eng. Mech. ASCE*, 119:1078 – 1098, 1993.

[9] Y. Li and A. Kareem. Stochastic decomposition and application to probabilistic dynamics. *J. Eng. Mech. ASCE*, 121:162 – 174, 1993.

[10] American Society of Civil Engineers Staff. *Minimum Design Loads for Buildings And Other Structures: Sei/asce 7-05*. Asce Standard No. 7-05. Amer Society of Civil Engineers, 2005.

[11] M. Di Paola. Digital simulation of wind field velocity. *Journal of Wind Engineering and Industrial Aerodynamics*, 74-76:91–109, 1998.

[12] M. Di Paola and I. V. Gullo. Digital generation of multivariate wind field processes. *Probabilistic Engineering Mechanics*, 16:1–10, 2001.

[13] E. Simiu and T. Miyata. *Design of Buildings And Bridges for Wind: A Practical Guide for Asce-7 Standard Users And Designers of Special Structures.* John Wiley, 2006.

[14] E. Simiu and R.H. Scanlan. *Wind Effects on Structures: Fundamentals and Applications to Design.* A Wiley-Interscience publication. John Wiley, 1996.

[15] E. Strømmen. *Theory of Bridge Aerodynamics.* Springer, 2010.

[16] Filippo Ubertini and Fabio Giuliano. Computer simulation of stochastic wind velocity fields for structural response analysis: Comparisons and applications, 2010.

[17] T. von Kármán. Progress in the statistical theory of turbulence. *Journal of marine research*, 7:252–264, 1948.

Appendix A

Appendix A

In this appendix the points in which the wind velocity simulations were generated are described in two tables giving the coordinates and node number in the FE-Model (table A.1), and the separation between adjacent points and coordinates used as input in NOWS (table A.2).

In table A.1 the desired x-value given in column 3 is the calculated x-values based on the mean separation between to adjacent points calculated from the end points. The "position of node" given in the second column indicates which cross section each nodes belongs to, where super refers to the superstructure. For the points along the superstructure there are two FEM node numbers, the first one referring to the windward girder and the latter to the leeward girder. The z-coordinate from Abaqus is not given here but it is $z = 0$ for the points along the arch, $z = +6.593$ for the points on the windward girder and $z = -6.593$ for the points on the leeward girder.

In table A.2 the separation of points is calculated as the sum of half the distance to each of the two adjacent points. The x and z coordinates are the input coordinates to the NatHaz On-line Wind Simulator (NOWS) [2]. The NOWS seems to assume that the points are located above a flat surface so the z-coordinate seems to be used both to define a points height over ground and to define the distance between points. The different cases for the different z values are given as follows:

z_1 Calculating an approximate real height under each point by approximating the surface to rise linearly between the sea and the arch abutments, and between each arch abutment and pier 5 and 8. The only exception to this is that the arch abutment on the Norwegian side (point

7A in figure 4.1) is blasted 7.437 m into the ground, so the linear rise here is from a point 7.437 m above the arc abutment and up to the abutment of pier 8. This approach gives more emphasis on getting the height correct and assume that this is more important than the correlation effects between the points.

z_2 Assuming the entire span between pier 5 and 8 lies over water. This would give correct correlation effects between points, but would give a bad representation of the height, particularly near pier 5 and 8, thus especially affecting the mean wind calculations.

z_3 A more conservative estimate than assuming the entire bridge lies over water would be to assume that the terrain under the bridge is uniformly distributed equal to the mean height of the terrain and the water surface, which is calculated to be 12.87 m.

z_4 The last approach is to set all the points over water to their correct value and to assume that the terrain has an equal height above the sea set to the mean value of the terrain height (24.10 m), and that this height is constant from the waterline and to pier 5 and 8. So the terrain is set to be constant of an height of 24.10 m above the waterline. This would be a sort of combinations between all of the approaches above, where the points to some degree have the correct height and to some degree have the correct separation between each other.

Table A.1: FEM coordinates and node numbers

Point no.	Position of node	Desired x-value	Abaqus coordinates		FEM node no.
			x	y	
1	Arch 1	−123.050	−122.046	−29.557	882
2	Arch 1	123.050	122.045	−29.557	836
3	Arch 1	−119.972	−118.727	−25.411	883
4	Arch 1	119.972	118.727	−25.411	835
5	Arch 1	−116.767	−115.268	−21.382	884
6	Arch 1	116.767	115.267	−21.382	834
7	Arch 1	−113.440	−111.672	−17.475	885
8	Arch 1	113.440	111.672	−17.475	833
9	Arch 1	−109.994	−109.824	−15.568	442

Point no.	Position of node	Desired x-value	Abaqus coordinates		FEM node no.
			x	y	
10	Arch 1	109.994	109.824	−15.568	404
11	Arch 1	−106.432	−106.032	−11.851	443
12	Arch 1	106.432	106.031	−11.852	403
13	Arch 2	−102.758	−102.113	−8.267	82
14	Arch 2	102.758	102.113	−8.268	68
15	Arch 2	−98.976	−97.847	−4.634	438
16	Arch 2	98.976	98.079	−4.825	837
17	Arch 2	−95.090	−93.451	−1.158	81
18	Arch 2	95.090	94.675	−2.100	843
19	Arch 2	−91.105	−89.060	2.066	435
20	Arch 2	91.105	90.528	1.014	842
21	Arch 2	−87.023	−86.822	3.619	877
22	Arch 2	87.023	86.280	3.987	841
23	Arch 2	−82.850	−82.266	6.606	878
24	Arch 2	82.850	81.933	6.815	840
25	Arch 2	−78.590	−77.608	9.430	879
26	Arch 2	78.590	77.495	9.495	839
27	Arch 3	−74.247	−73.096	11.957	873
28	Arch 3	74.247	72.816	12.107	845
29	Arch 3	−69.827	−68.749	14.208	874
30	Arch 3	69.827	70.366	13.391	413
31	Arch 3	−65.332	−66.550	15.282	434
32	Arch 3	65.332	65.399	15.826	71
33	Arch 3	−60.770	−60.000	18.230	869
34	Arch 3	60.770	60.392	18.063	416
35	Arch 3	−56.143	−55.755	19.948	870
36	Arch 3	56.143	55.309	20.120	415
37	Arch 3	−51.458	−51.462	21.540	871
38	Arch 3	51.458	52.741	21.081	847
39	Arch 3	−46.718	−47.124	23.003	872
40	Arch 3	46.718	47.555	22.864	846
41	Arch 4	−41.929	−42.867	24.302	867
42	Arch 4	41.929	42.425	24.429	850

Point no.	Position of node	Desired x-value	Abaqus coordinates		FEM node no.
			x	y	
43	Arch 4	-37.096	-36.601	25.973	77
44	Arch 4	37.096	37.388	25.778	855
45	Arch 4	-32.224	-32.208	26.979	425
46	Arch 4	32.224	32.335	26.951	854
47	Arch 4	-27.319	-27.788	27.855	426
48	Arch 4	27.319	27.245	27.953	853
49	Arch 4	-22.384	-23.343	28.602	427
50	Arch 4	22.384	22.125	28.784	852
51	Arch 4	-17.426	-16.641	29.479	866
52	Arch 4	17.426	16.979	29.441	851
53	Arch 5	-12.450	-12.751	29.851	861
54	Arch 5	12.450	11.855	29.923	860
55	Arch 5	-7.461	-8.553	30.142	856
56	Arch 5	7.461	6.759	30.231	859
57	Arch 5	-2.463	-3.451	30.340	857
58	Arch 5	2.463	1.655	30.370	858
59	Arch 5	0	-0.898	30.376	422
60	Super	-162.814	-162.814	-0.227	22, 20
61	Super	-154.591	-155.382	-0.327	715, 531
62	Super	-146.368	-145.473	-0.460	713, 533
63	Super	-138.145	-138.041	-0.559	300, 163
64	Super	-129.922	-130.610	-0.659	710, 536
65	Super	-121.699	-120.701	-0.792	708, 538
66	Super	-113.476	-113.269	-0.892	295, 168
67	Super	-105.253	-105.837	-0.991	705, 541
68	Super	-97.030	-93.451	-1.158	56, 19
69	Super	-88.807	-88.229	-1.228	309, 154
70	Super	-80.584	-80.396	-1.333	720, 526
71	Super	-72.361	-72.563	-1.438	306, 157
72	Super	-64.138	-64.731	-1.543	717, 529
73	Super	-55.915	-57.020	-1.646	274, 150
74	Super	-47.692	-46.821	-1.783	272, 152
75	Super	-39.469	-39.172	-1.886	676, 523

Point no.	Position of node	Desired x-value	Abaqus coordinates		FEM node no.
			x	y	
76	Super	-31.246	-31.522	-1.988	$384, 146$
77	Super	-23.023	-23.873	-2.091	$806, 516$
78	Super	-14.800	-13.674	-2.228	$804, 518$
79	Super	-6.577	-6.025	-2.331	$265, 142$
80	Super	1.646	1.625	-2.433	$661, 511$
81	Super	9.869	9.274	-2.536	$262, 145$
82	Super	18.092	16.923	-2.638	$785, 504$
83	Super	26.315	27.122	-2.775	$783, 506$
84	Super	34.538	34.772	-2.878	$362, 141$
85	Super	42.761	42.421	-2.981	$646, 499$
86	Super	50.984	50.070	-3.083	$255, 135$
87	Super	59.207	60.269	-3.220	$253, 137$
88	Super	67.430	67.981	-3.323	$772, 493$
89	Super	75.653	75.815	-3.429	$354, 130$
90	Super	83.876	83.650	-3.534	$769, 496$
91	Super	92.099	91.485	-3.639	$351, 133$
92	Super	100.322	96.708	-3.709	$33, 12$
93	Super	108.545	109.100	-3.875	$622, 481$
94	Super	116.768	116.536	-3.975	$236, 119$
95	Super	124.991	123.971	-4.075	$619, 484$
96	Super	133.214	133.885	-4.208	$617, 486$
97	Super	141.437	141.321	-4.307	$231, 124$
98	Super	149.660	148.756	-4.407	$614, 489$
99	Super	157.833	158.670	-4.540	$612, 491$
100	Super	166.106	166.106	-4.634	$9, 11$

Table A.2: Separation between points and input coordinates to NOWS

Point no.	Separation of points	Input coordinates to NOWS				
		x	z_1	z_2	z_3	z_4
1	3.908	-122.046	2.955	30.415	17.542	6.312
2	3.908	122.045	3.251	30.415	17.542	6.312
3	5.311	-118.727	8.838	34.561	21.688	10.458
4	5.311	118.727	9.745	34.561	21.688	10.458

Point	Separation	Input coordinates to NOWS				
no.	of points	x	z_1	z_2	z_3	z_4
5	5.311	−115.268	14.678	38.590	25.717	14.487
6	5.311	115.267	16.221	38.589	25.716	14.486
7	3.983	−111.672	20.467	42.497	29.624	18.394
8	3.982	111.672	22.673	42.497	29.624	18.394
9	3.982	−109.824	23.343	44.404	31.531	20.301
10	3.983	109.824	25.888	44.404	31.531	20.301
11	5.310	−106.032	39.043	48.121	35.248	24.018
12	5.310	106.031	32.288	48.120	35.247	24.017
13	5.457	−102.113	34.679	51.705	38.832	27.602
14	5.307	102.113	38.645	51.704	38.831	27.601
15	5.604	−97.847	40.545	55.338	42.465	31.235
16	4.832	98.079	44.943	55.147	42.274	31.044
17	5.526	−93.451	46.322	58.814	45.941	34.711
18	4.774	94.675	50.076	57.872	44.999	33.769
19	4.086	−89.060	51.844	62.038	49.165	37.935
20	5.186	90.528	56.125	60.986	48.113	36.883
21	4.086	−86.822	54.569	63.591	50.718	39.488
22	5.186	86.280	62.104	63.959	51.086	39.856
23	5.448	−82.266	59.940	66.578	53.705	42.475
24	5.186	81.933	66.787	66.787	53.914	66.787
25	5.310	−77.608	65.202	69.402	56.529	45.299
26	5.272	77.495	69.467	69.467	56.594	69.467
27	5.034	−73.096	70.091	71.929	59.056	47.826
28	4.062	72.816	72.079	72.079	59.206	72.079
29	3.671	−68.749	74.180	74.180	61.307	74.180
30	4.149	70.366	73.363	73.363	60.490	73.363
31	4.815	−66.550	75.254	75.254	62.381	75.254
32	5.508	65.399	75.798	75.798	62.925	75.798
33	5.882	−60.000	78.202	78.202	65.329	78.202
34	5.484	60.392	78.035	78.035	65.162	78.035
35	4.579	−55.755	79.920	79.920	67.047	79.920
36	4.113	55.309	80.092	80.092	67.219	80.092
37	4.579	−51.462	81.512	81.512	68.639	81.512

Point	Separation	Input coordinates to NOWS				
no.	of points	x	z_1	z_2	z_3	z_4
38	4.112	52.741	81.053	81.053	68.180	81.053
39	4.515	−47.124	82.975	82.975	70.102	82.975
40	5.424	47.555	82.836	82.836	69.963	82.836
41	5.468	−42.867	84.274	84.274	71.401	82.836
42	5.289	42.425	84.401	84.401	71.528	84.401
43	5.496	−36.601	85.945	85.945	73.072	85.945
44	5.201	37.388	85.750	85.750	72.877	85.750
45	4.506	−32.208	86.951	86.951	74.078	86.951
46	5.188	32.335	86.923	86.923	74.050	86.923
47	4.507	−27.788	87.827	87.827	74.954	87.827
48	5.188	27.245	87.925	87.925	75.052	87.925
49	5.634	−23.343	88.574	88.574	75.701	88.574
50	5.188	22.125	88.756	88.756	75.883	88.756
51	5.334	−16.641	89.451	89.451	76.578	89.451
52	5.167	16.979	89.413	89.413	76.540	89.413
53	4.058	−12.751	89.823	89.823	76.950	89.823
54	5.126	11.855	89.895	89.895	77.022	89.895
55	4.657	−8.553	90.114	90.114	77.241	90.114
56	5.106	6.759	90.203	90.203	77.330	90.203
57	3.830	−3.451	90.312	90.312	77.439	90.312
58	2.932	1.655	90.342	90.342	77.469	90.342
59	1.655	−0.898	90.348	90.348	77.475	90.348
60	7.432	−162.814	16.745	59.745	46.872	35.642
61	8.671	−155.382	19.435	59.645	46.772	35.542
62	8.671	−145.473	23.021	59.512	46.639	35.409
63	7.432	−138.041	25.712	59.413	46.540	35.310
64	8.670	−130.610	28.401	59.313	46.440	35.210
65	8.671	−120.701	32.424	59.180	46.307	35.077
66	7.432	−113.269	36.214	59.080	46.207	34.977
67	9.909	−105.837	40.005	58.981	46.108	34.878
68	8.804	−93.451	46.322	58.814	45.941	34.711
69	6.528	−88.229	48.985	58.744	45.871	34.641
70	7.833	−80.396	52.890	58.639	45.766	34.536

Point	Separation	Input coordinates to NOWS				
no.	of points	x	z_1	z_2	z_3	z_4
71	7.833	-72.563	56.534	58.534	45.661	34.431
72	7.772	-64.731	54.429	58.429	45.556	58.429
73	8.955	-57.020	56.326	58.326	45.453	58.326
74	9.924	-46.821	56.189	58.189	45.316	58.189
75	7.650	-39.172	56.086	58.086	45.213	58.086
76	7.650	-31.522	55.984	57.984	45.111	57.984
77	8.924	-23.873	55.881	57.881	45.008	57.881
78	8.924	-13.674	55.744	57.744	44.871	57.744
79	7.650	-6.025	55.641	57.641	44.768	57.641
80	7.650	1.625	55.539	57.539	44.666	57.539
81	7.649	9.274	55.436	57.436	44.563	57.436
82	8.924	16.923	55.334	57.334	44.461	57.334
83	8.925	27.122	55.197	57.197	44.324	57.197
84	7.650	34.772	55.094	57.094	44.221	57.094
85	7.649	42.421	54.991	56.991	44.118	56.991
86	7.649	50.070	54.889	56.889	44.016	56.889
87	8.956	60.269	54.752	56.752	43.879	56.752
88	7.773	67.981	54.649	56.649	43.776	56.649
89	7.835	75.815	54.543	56.543	43.670	56.543
90	7.835	83.650	54.438	56.438	43.565	56.438
91	6.529	91.485	50.795	56.333	43.460	32.230
92	8.808	96.708	47.029	56.263	43.390	32.160
93	9.914	109.100	38.093	56.097	43.224	31.994
94	7.435	116.536	32.731	55.997	43.124	31.894
95	8.675	123.971	27.488	55.897	43.024	31.794
96	8.675	133.885	23.993	55.764	42.891	31.661
97	7.434	141.321	21.371	55.665	42.792	31.562
98	8.675	148.756	18.750	55.565	42.692	31.462
99	8.675	158.670	15.254	55.432	42.559	31.329
100	7.436	166.106	12.638	55.338	42.465	31.235

Appendix B

Appendix B

In this appendix data for the drag coefficient from the wind tunnel test is presented. First two figures are given to show the definition of positive directions of the drag force (see fig. B.1 and fig. B.2). Then follows two figures showing diagrams of the measured results of the wind tunnel test (see fig. B.3 and fig. B.4).

The formula used to determine the drag coefficoent is the following:

$$C_D = \frac{D}{\rho/2v^2B}$$

where ρ is the density of air ($1.28\,\text{kg/m}^3$ for prototype), v is the velocity in m/s (mean velocity in the wind tunnel) and B is the width of the cross section ($27.60\,\text{m}$ in full scale).
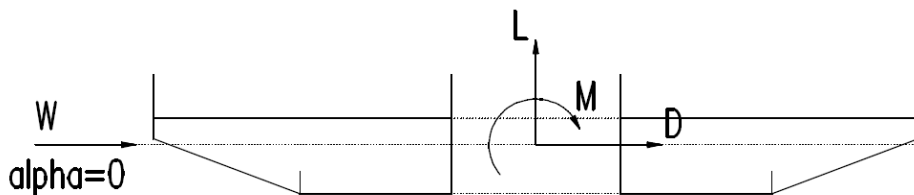
Figure B.1: Definition of positive directions of Lift (L), Drag (D) and Moment (M) for an onflow angle (inclination) of $0°$. Taken from [6].
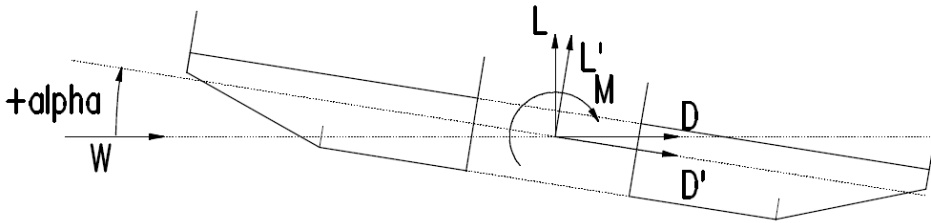
Figure B.2: Definition of positive directions of Lift (L), Drag (D) and Moment (M) for an positive onflow angle (inclination $>0°$).The forces in the body fixed coordinate system are indicated with L' and D'. Taken from [6].
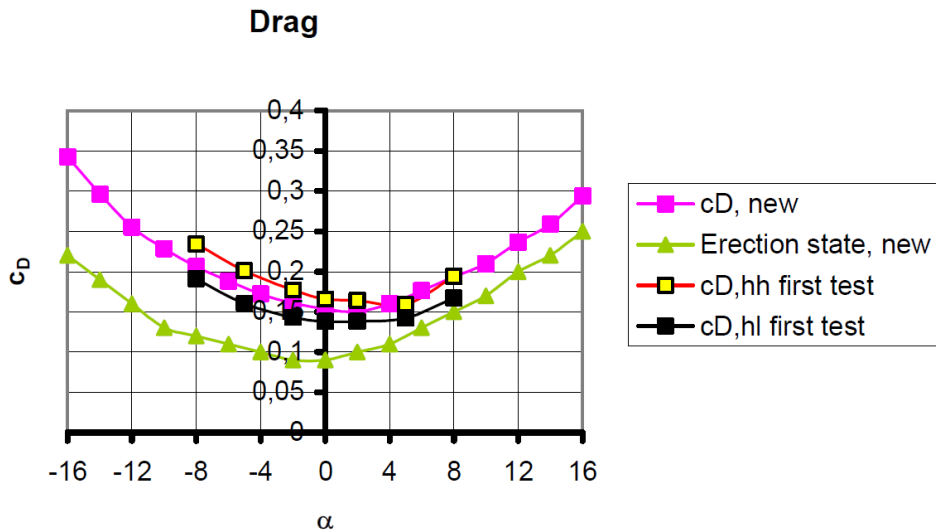

Figure B.3: Drag coefficients versus onflow angle α for the final cross section (new), the final cross section without screen (used in construction phase, erection) and comparison with previous data. Taken from [6].
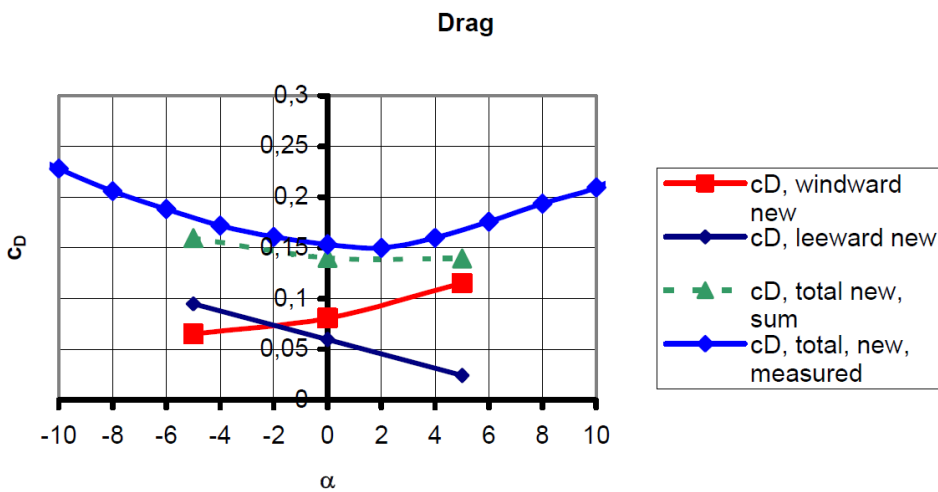
Drag

Figure B.4: Drag coefficients versus onflow angle α for the final cross section with screen, and each girder separately, (dotted line: result of summation). Taken from [6].

Appendix C

Appendix C

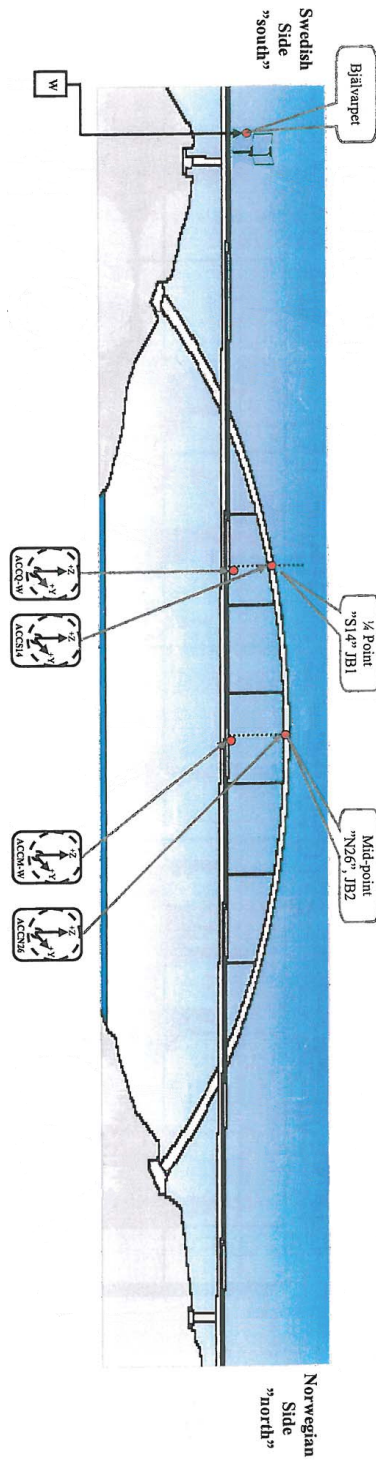On the next pace a larger vertical alligned version of figure 5.1 is given.

Figure C.1: Placement of sensors